

SYNTHESIS AND FUNCTIONALIZATION OF d-PLL-PEG-FA COATED GOLD
NANOPARTICLES FOR siRNA DELIVERY IN HUMAN PROSTATE CANCER

A Thesis
presented to
the Faculty of Natural and Applied Sciences
at Notre Dame University-Louaize

In Partial Fulfillment
of the Requirements for the Degree
Master of Science in Biology

by
GEORGES B. MINASSIAN

SPRING 2021

© COPYRIGHT

By

Georges B. Minassian

2021

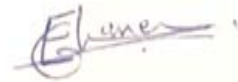
All Rights Reserved

Notre Dame University - Louaize
Faculty of Natural & Applied Sciences
Department of Sciences

We hereby approve the thesis of

Georges B. Minassian

Candidate for the degree of Master of Science in Biology



Dr. Esther Ghanem

Supervisor, Chair



Dr. Kamil Rahme

Committee Member



Dr. Pauline Aad

Committee Member

Table of contents

Abstract	iv
Acknowledgements	6
List of tables and figures	8
Abstract	10
I. Introduction	11
II. Literature Review	15
A. Background on Prostate Cancer	16
B. Causes, Risk Factors, and Symptoms	17
C. Screening and Diagnosis of Prostate Cancer	18
D. Current Treatments	18
E. Targeted Therapy, Nanotechnology, and Prostate Cancer	19
F. Prostate-Specific Membrane Antigen (PSMA) and Prostate Cancer.....	20
G. PC3 cell line.....	21
H. Various NPs and their Theranostic Applications in Prostate Cancer.....	21
i. <i>Liposomes</i>	22
ii. <i>Quantum Dots</i>	23
iii. <i>Gadolinium and Manganese NPs</i>	24
iv. <i>Silver and Platinum NPs</i>	25
v. <i>Iron Oxide NPs</i>	26
I. Gold Nanoparticles (AuNPs) Characteristics and use in Prostate Cancer	27
i. <i>Characteristics</i>	27
ii. <i>AuNPs for PSA detection</i>	28
iii. <i>AuNPs as active targeting theranostics</i>	29
iv. <i>AuNPs as Imaging Enhancers</i>	30
J. Dendritic Poly-L-Lysine: Importance and role.....	31
K. Importance of siRNA and Folate Receptors in Prostate Cancer	33
III. Materials and Methods	36
IV. Results	44
V. Discussion	52
VI. Conclusion and Future Perspectives	58
VII. References	82

Acknowledgements

My most profound acknowledgments are extended to the following:

I would like to deeply express my gratitude towards my supervisor, **Dr. Esther Ghanem**.

Since my curiosity and potential piqued your interest, you took me under your wing and taught me everything you could, throughout my long journey at NDU.

Without your constant guidance, support, positive, and professional critique, I would never have made it this far. Hundreds of hours were spent brainstorming, developing techniques, and testing in the lab. You taught me patience, and how to properly think outside the box. The researcher I am today, is a cumulation of all the knowledge, arduous work, and expertise you shared with me.

My most cordial thanks to **Dr. Kamil Rahme**, Chairperson of the Department of Sciences, FNAS, NDU.

The three years I spent under your supervision, as your Research Assistant will never be forgotten. You taught me the meaning of Interdisciplinary work. Your firm guidance and resolution, allowed me, a Biologist, to perform complicated chemical syntheses, that were proven to be crucial for our work. Thank you for always being there when I needed you, for all your support, and vital input. You taught me that proper research is conducted through the right collaborations. A lesson I will never forget.

I would also like to deeply thank **Dr. Pauline Aad** for all her assistance, precious insight, and for being a member of my thesis committee.

A major thank you goes to **Mrs. Nada Maalouf, Mrs. Rita El-Am El- Hajj, Mrs. Elizabeth Saliba, and Ms. Simona Sawan**. You were, and always will be one of the key elements of our success. You often spent numerous hours at the lab guiding us, helping us improve on our work, and tending to all our needs. I thank you all from the bottom of my heart for always supporting us academically and emotionally.

I would also like to acknowledge **Dr. Gulio Fracasso** for the kind donation of the PC3-PSMA cell line used in this work.

Finally, I would like to thank, **Dr. Colette Kabrita** for accompanying me along this ride, as my Student Advisor. Thank you for always being there and for helping me navigate through all the administrative obstacles I faced as a student.

List of tables and figures

Tables

Table 1. Characterization of AuNPs-d-PLL, AuNPs-d-PLL-PEG, and AuNPs-d-PLL-FA via Dynamic Light Scattering and ZETA measurements. Readings were performed in triplicates in disposable folded capillary tubes (n = 3).

Table 2. Characterization of AuNPs-d-PLL, PEG, and FA for siRNA Delivery via Dynamic Light Scattering, ZETA measurements and UV-Vis Spectrophotometry. Readings were performed in triplicates in disposable folded capillary tubes (n = 3).

Figures

Figure 1. Effect of increasing [HAuCl₄] on Size Distribution by Intensity of AuNPs-d-PLL.

Figure 2. Effect of increasing [d-PLL] on Size Distribution by Intensity of AuNPs-d-PLL.

Figure 3. Effect of increasing [Asc Ac] on Size Distribution by Intensity of AuNPs-d-PLL.

Figure 4. Effect of increasing [HAuCl₄] on Zeta Potential of AuNPs-d-PLL.

Figure 5. Effect of increasing [d-PLL] on Zeta Potential of AuNPs-d-PLL.

Figure 6. Effect of increasing [Asc Ac] on Zeta Potential of AuNPs-d-PLL.

Figure 7. Size distribution by Intensity of AuNPs-d-PLL Vs. AuNPs-d-PLL-PEG-OCH₃ and AuNPs-d-PLL-PEG-FA.

Figure 8. Zeta measurements of AuNPs-d-PLL Vs. AuNPs-d-PLL-PEG-OCH₃ and AuNPs-d-PLL-PEG-FA.

Figure 9. Uv-Vis spectra of AuNPs-d-PLL, AuNPs-d-PLL-PEG, and AuNPs-d-PLL-PEG-FA.

Figure 10. Uv-Vis Spectra of AuNPs-d-PLL Synthesized with Increasing HAuCl₄ Concentrations.

Figure 11. Uv-Vis Spectra of AuNPs-d-PLL Synthesized with Increasing d-PLL Concentrations.

Figure 12. UV-Vis Spectra of AuNPs-d-PLL Synthesized with Increasing Asc Ac Concentrations.

Figure 13. WST-1 Cell Proliferation Assay of AuNPs-d-PLL-PEG-FA.

Figure 14. Agarose gel electrophoresis of various AuNPs.siRNA MRs captured under UV light with ChemiDoc™.

Figure 15. Mean Percent Fluorescence of AuNPs-d-PLL-PEG OCH₃ vs. AuNPs-d-PLL-PEG-FA.

Figure 16. siRNA Intracellular Localization.

Figure 17. Z-stack imaging of PSMA cells treated with AuNPs-PEG.siRNA (50 nM)s Vs. AuNPs-PEG-FA.siRNA (50 nM).

Abstract

Herein, we describe, a simple method for the synthesis of dendrigraft poly-L-lysine (d-PLL) coated gold nanoparticles in water (AuNPs-d-PLL) as potential vehicles of siRNA delivery to prostate cancer cells, PC3-PSMA. AuNPs-d-PLL with diameters ranging between 50–130 nm have been synthesized in aqueous solutions using d-PLL (7 KD) as a capping ligand and L-ascorbic acid as a reducing agent. The size of the resulting AuNPs was found to depend on several parameters, such as the concentrations of gold salt, reducing agent, and d-PLL. The obtained AuNPs-d-PLL were characterized using UV-visible spectroscopy (UV-vis) and Dynamic Light Scattering (DLS). Increasing the concentration of the gold precursor (HAuCl₄) resulted in an overall increase in AuNP size (Z avg). On the other hand, an increase in reducing agent concentration resulted in a decrease in average particle size. Concerning the increase in capping agent (d-PLL), no significant change on AuNPs size was observed. Furthermore, the ability to PEGylate the AuNPs-d-PLL with SH-PEG-OCH₃ and SH-PEG-Folate was demonstrated via DLS and zeta potential measurements, their capacity to complex siRNA was verified using DLS and gel electrophoresis. Finally, transfer of AuNPs-d-PLL-PEG-FA.siRNA to PC3-PSMA cells was investigated via FACS, laser scanning microscopy, and Z-stacking.

Keywords: gold nanoparticles, polymers, stabilization, siRNA delivery, cancer

I. Introduction

Prostate cancer (PC) is the second leading cause of death in men. According to the American Cancer Society's latest data in 2021, around 248,530 new cases of prostate cancer were diagnosed, while about 34,130 deaths have been attributed to the disease[1][2]. siRNA delivery has potential use in cancer treatment as it is well known to selectively down-regulate genes implicated in tumor cell proliferation [3]. Use of unprotected siRNA in therapeutics must overcome several barriers. For example, naked siRNA suffer from a short plasma half-lifetime caused mainly by enzymatic degradation by serum endonucleases and RNAases. Furthermore, rapid renal clearance, and membrane impermeability originated from their electrostatic repulsion by the negatively charged phospholipidic cell membrane, retards their uptake by targeted cells [4, 5]. Therefore, to overcome the abovementioned barriers several strategies were investigated for improving the use of siRNA in therapeutics [6]. Among the strategies that are aiming to increase the retention time of siRNA in the body, conjugating siRNA onto nanoparticles (NPs) has been lately a hotspot in research to improve siRNA-based treatment in cancer [7, 8]. It has been demonstrated that NPs-siRNA cargos can shield naked siRNA from degradation, renal clearance, and reticuloendothelial system (RES) entrapment [4]. Moreover, NPs offer the ability of longer circulation in blood stream as well as it can be further modified with small molecules targeting ligands that can specifically recognize a tumor cell surface receptor [9, 10]. Therefore, several lipids and polymer-based nanoparticles were used as vehicles in siRNA delivery to cancer cells [11]. Moreover, it has been demonstrated that positively charged nanoparticles can display increased interactions with cell membranes that result in an enhanced endocytosis [12, 13]. Among other nanocarriers, gold nanoparticles (AuNPs) are known for their size and shape dependent optical properties, low cytotoxicity, and high affinity to thiols and amines that facilitate their modification with biomolecules such as antibodies, proteins, and thiol terminated ligands [14, 15]. AuNPs are now widely used in biomedical applications such as bioimaging, photothermal therapy, drug, and gene delivery vehicles [16]. In order to be successfully used in siRNA delivery, AuNPs should exhibit a positively charged surface allowing

them to successfully and electrostatically complex the negatively charged siRNA. In a previous study, it has been demonstrated that positively charged AuNPs could be easily obtained using L-cysteine and polyethyleneimine (PEI) as capping ligands, with both AuNPs were found to be not cytotoxic when tested *in-vitro* [5, 17]. PEI is now widely used in the delivery of siRNA, since it was demonstrated that PEI becomes protonated at low intracellular pH, hence facilitating endosomal escape and destabilization of endosomal membranes [17-19]. Previously, it has been reported that AuNPs-PEI 2KD and AuNP-PEI 25KD could both successfully complex siRNA, and the latter (25 KD) only could deliver siRNA into PC3 cancer cells (~98 %) without further modification with a targeting ligand [12]. Moreover, it has also been demonstrated that the very low uptake of AuNPs-PEI 2KD could be enhanced by modification with a targeting ligand, such as Anisic Acid (AA) or Folic acid (FA) [15, 18]. Au-PEI-AA mediated efficient siRNA uptake into PC3 prostate cancer cells via binding to the sigma receptor and resulted in highly efficient knockdown of the Rel A gene (70%) when cells were transfected in serum-free medium [18]. Similarly, the AuNPs-PEI-FA.siRNA specifically delivered siRNA into LNCaP cells, a PC cell line overexpressing prostate specific membrane antigen (PSMA). This receptor exhibits a hydrolase enzymatic activity with a folate substrate and produced an enhanced endogenous gene silencing compared to the non-targeted AuNPs-PEI [15]. However, results also demonstrated that AuNPs-PEI-FA size was found to increase by threefold after siRNA complexation, mainly due to some flocculation upon siRNA addition. Therefore, we believe that PEGylation might be of interest to enhance AuNPs stability as well as their circulation time *in vivo*.

In this presented work, we used dendrigraft poly (L-lysine) (d-PLL) as a stabilizing ligand for gold AuNPs in water. The d-PLL generation two (P2) with a narrow molecular weight distribution of about 7 KDa was obtained by a previously reported method [20]. AuNPs-d-PLL with diameters ranging between 50 – 130 nm could be obtained by chemical reduction of tetra chloroauric acid (HAuCl₄) with L-ascorbic acid in the presence of d-PLL. Furthermore, the effect of increasing concentrations of d-PLL,

L-ascorbic acid and HAuCl_4 on AuNP synthesis were investigated. AuNPs-d-PLL presenting a hydrodynamic diameter of 110 nm were chosen and further modified with SH-PEG5000-OCH₃ (Mw 5400 g.mol⁻¹) or SH-PEG5000-FA. Successful PEGylation was confirmed by DLS and zeta potential measurements. The resulting PEGylated AuNPs-d-PLL were shown to complex siRNA and folate modified ones could deliver siRNA to PC3 PSMA cells. Indeed, agarose gel electrophoresis demonstrated that our NPs were able to successfully complex siRNA at MR 20 and 30. Furthermore, the binding ability of our nanocomplex against PSMA was tested using FACS, with ~ 30% of AuNPs-d-PLL-PEG-FA.siRNA exhibiting specific binding to PSMA receptors on PC3 cells. Finally, the internalization profile of our NPs was investigated via laser scanning microscopy, with Z-stack imaging confirming the inter-cytoplasmic presence of our nano-vehicles when incubated with PSMA positive PC3 cells *in-vitro*.

II. Literature Review

A. Background on Prostate Cancer

The prostate is a small walnut-sized, 3 cm gland [21]. It is situated at the base of the penis, adhering firmly to the bottom of the bladder [22]. The gland has a fundamental role in producing and secreting 30 to 35 % of the semen's fluid, while the rest is composed of seminal fluid secreted by the seminiferous tubules, enzymes, and lipids [21, 22]. This fluid mainly serves as a shield and sustenance to the sperm, while also providing necessary alkaline pH [22, 23].

Unfortunately, PC is the most common type of malignancy affecting the male population. [24]. It has been described as the second most frequently diagnosed cancer in men and ranked sixth in the increasing order of deadly cancers among that population [24, 25]. The malignancy is described by prostate cells undergoing genetic mutations, followed by the abnormal growth of cancer cells, leading to tumor development and subsequent hyperplasia [26]. On the other hand, PC development is usually slow with inferior risk and low to moderate aggressiveness [27]. PC development becomes aggressive upon reaching metastasis. This is when the malignancy extends to the bones, lymph nodes, and lungs [28]. The main risk factors for prostate cancer are classified as age, ethnicity, obesity, and family history [29].

Most PCs are adenocarcinomas having indefinite tumor cell growth complemented with the disappearance of basal cells [30]. These adenocarcinomas exhibit glandular formations and express a variety of specific receptors, namely androgen receptor (AR), prostate-specific antigen (PSA), and prostate-specific membrane antigen (PSMA) [31]. However, in benign prostate, malignancy can occur with around 1% of neuroendocrine tumor cells, not expressing AR and PSA [32, 33].

Because of its dependency on androgens, anti-testosterone hormonal therapy proved effective against PC. However, many cases exist where malignant adenocarcinomas resist chemical castration. These tumors are believed to produce androgens intracellularly [34]. Therefore, the development of

more specific and targeted therapies should be prioritized. Currently, many targeted therapies are being developed against PC with promising results, such as radio-immunotherapy (RIT) [35, 36]. These techniques have exhibited successful toxicity against malignant tumors and offer to increase the survival rate of afflicted patients [37].

B. Causes, Risk Factors, and Symptoms

The main key elements underlying PC development remain elusive. However, many risk factors have been attributed to its occurrence, such as age, family history, and obesity [38]. Additionally, prostatic adenocarcinomas are highly correlated with age [39, 40]. High-risk patients are men above the age of 65 with median age of PC mortality at 81 years [41]. In parallel, multiple cohort and patient case studies from diverse populations claim that a primary risk of PC is family history [42-44]. The risk is even higher if a male sibling or paternal link is afflicted, while also being inversely associated with the age of that afflicted family member [42, 44-46]. Alternatively, Kolonel et.al, 2004 reported other exogenous contributors such as alcohol intake, diet, and frequency of intercourse that might impact the development and prognosis of PC [47].

With regards to symptoms, PC is considered asymptomatic in its early stages. In opposition, the disease might exhibit minor symptoms, such as frequent urination, nocturia, hematuria and dysuria [48]. Furthermore, the disease can illicit trouble regarding sexual performance, with patients experiencing erectile dysfunction and pain during ejaculation [49]. Moreover, the malignancy is responsible for a major consequence termed spinal cord compression, which is responsible for a multitude of symptoms, such as leg weakness, tingling, pain, paralysis, urinary, and fecal incontinence [50]. Finally, unbearable bone pain in the vertebrae, pelvis, hips, or lower ribs, is usually experienced during PC metastasis with the spread reaching into the proximal part of the femur [51].

C. Screening and Diagnosis of Prostate Cancer

The sinister behavior of PC poses an immense problem regarding early diagnosis. Patients are often diagnosed at later stages of the malignancy, despite the substantial technological advances in adenocarcinoma detection [41, 44, 47, 52, 53]. Three main techniques are employed when screening for prostate malignancy: Digital Rectal Examination (DRE), which detects the disease only at late stages [54], PSA blood testing, and a prostate gland biopsy [55]. Abnormal tissue and bone morphology are often detected using conventional imaging techniques, such as ultrasound, MRI, and CT scans [40].

Nowadays, regular testing for PSA is thought to reduce the chance of succumbing to PC [41]. PSA is a kallikrein-like serine protease produced by the epithelial cells of the prostate [44]. It has a molecular weight of 34 kDa and can easily be detected in the bloodstream [56]. A PSA level of 4.0 ng/mL is viewed as a sensible threshold for additional assessment. Nevertheless, there is no evident PSA cutoff point distinguishing between PC and a healthy gland [41]. Also, recent findings have shown that few men with PSA levels underneath 4.0 ng/mL have prostate malignancy and that numerous men with more significant levels remain healthy [57]. Recognizing this obstacle, patients are frequently guided to take the additional step of X-ray testing, trans-rectal ultrasound assessment, and cystoscopy to conclude the presence of prostate adenocarcinoma [37].

D. Current Treatments

Various treatments for PC do exist, however, they have essentially been witnessed to lead to variable adverse side effects [58] In general, an active observation is appropriate for patients diagnosed with low-risk PC. These patients are only treated when the tumor advances with time [59, 60] and over 80% capitulate to the malignancy after metastasis spreads to the bone [61]. Surgery is predominantly

recommended for locally advanced high-risk prostate carcinomas [62]. Radical prostatectomy and pelvic lymphadenectomy are regularly performed types of PC surgery [63].

Second after surgery is radiotherapy. It is used for localized high-risk prostate cancers [64]. Hormonal, chemotherapeutic, or combination treatment choices are customarily alluded to when the malignancy is advanced and has metastasized to other neighboring tissues.

Thirdly, androgen deprivation therapy (ADT) is primarily employed medically or surgically, for the treatment of metastatic PC [65]. Treatments at this stage are only employed to alleviate the symptoms of the disease [58]. Also, the significant drawback of chemotherapy lies in the non-selective and random uptake of therapeutics by healthy cells [66].

In recent times, nanoparticles have emerged as the future key participants in diagnosis and treatment of prostatic adenocarcinomas [67]. These particles “shine the light at the end of the tunnel” for afflicted patients, by offering potentially safer and successful alternatives than the above mentioned therapeutic options.

E. Targeted Therapy, Nanotechnology, and Prostate Cancer

Nanotechnology has swiftly surfaced in the field of medical imaging and targeted drug delivery [68]. Research on developing such particles has enthusiastically increased in the past few years [37]. In current biomedical research, successful delivery of theranostics and therapeutic agents, or increasing their bioavailability to solid tumors, remains a challenge. However, by employing nanoparticles (NPs), this hurdle can be eliminated and even resolved [28].

One advantage displayed by targeted delivery is the ability to specifically deliver a treatment to malignant tissues [69]. This characteristic offers an enhanced and safer alternative to orthodox chemotherapeutics, by diminishing adverse side effects and overall toxicity to unaffected cells [70].

Furthermore, chemotherapy offers adequately low benefits to the patients, which are even outweighed by the risk of treatment, further highlighting the importance of targeted nano-therapies [71]. Moreover, it is crucial to design and synthesize a drug delivery vector with clinically approved components and the ability to circulate the blood for a long duration, to overcome cancer and its mutation chance [72]. In targeted therapy, having a uniquely overexpressed antigen on the tumor of interest is of vital importance since it ensures specific delivery of the drugs and spares healthy tissue. In PC, one overexpressed antigen is PSMA [73, 74].

F. Prostate-Specific Membrane Antigen (PSMA) and Prostate Cancer

PSMA was originally discovered by the monoclonal antibody (mAb) 7E11-C5 against human prostate adenocarcinoma cell line LNCaP [75]. It has a special tertiary structure: a 19-amino-acid internal portion, a 24-amino-acid transmembrane section, and a 707-amino-acid external section [76, 77]. It is a transmembrane folate hydrolase/carboxypeptidase involved in nutrient uptake by prostate cells [78]. The PSMA gene is situated on the short arm of chromosome 11, a region which is not subject to deletion during malignancy [79]. According to the literature, PSMA is expressed in all prostate cancers.

The exact role of PSMA and its implication in prostate adenocarcinoma progression remains obscured. However, this surface-bound protein increases its expression gradationally in higher-stage tumors [80]. Many experts have stipulated that PSMA plays a role as agonist to some integrins (e.g., $\alpha 2\beta 1$, $\alpha 3\beta 1$), and focal adhesion kinase signaling to enhance endothelial cell activation and angiogenesis [81]. Moreover, evidence suggests that PSMA might regulate the expression of interleukin-6 and the chemokine CCL5 by activating the MAPK pathway.

Being membrane bound, highly expressed on most PC cells and barely expressed on benign tissues, makes PSMA an ideal candidate for targeted therapy [72]. Furthermore, PSMA possesses an

internalization motif which facilitates cellular entry and concentration of delivery agents. Finally, PSMA is fundamentally endocytosed upon ligand induced binding, resulting in its intracellular recycling, and marking it as a prime candidate for specific targeted therapy against PC [82, 83].

G. PC3 cell line

The PC3 cell line originated in 1979, from a biopsy retrieved from a 62-year-old Caucasian male with metastatic PC to the bone [84]. The line is aneuploidy with a karyotype modal number of 58 and a generation time of approximately 33 hours. Furthermore, PC3 cells express elevated transferrin receptors and stimulated growth once exposed to transferrin of bone marrow origin [85, 86].

It is highly metastatic when compared to various other PC cell line models such as DU145 or LNCaP cells [87, 88]. In scientific research, PC3 mimics androgen independent prostate adenocarcinoma. Interestingly, the cells do not express AR and PSA, do not respond to androgens, glucocorticoids, epidermal, nor fibroblast growth factors, with significant independence on serum for growth [84, 89].

Finally, PC3 expresses abnormal p53 coupled with a deleted cytosine at codon 138. This mutation results in a nonsense codon at 169 accompanied by PTEN deficiency [89, 90]. Phosphatase and tensin homolog gene, PTEN, acts as a tumor suppressor gene in humans and is one of the most mutated genes in cancer [91-93].

H. Various NPs and their Theranostic Applications in Prostate Cancer

In recent years, the synthesis and bio-application of a multitude of metal and non-metal-based NPs, commonly under the size of 100 nm, has increased tremendously [94]. Nanotechnology is characterized by two main objectives the first concerning optimal drug loading capacity, and the second being enhanced blood circulation and specificity, considerably lowering the unwanted risk of toxic side effects

to healthy cells and enhancing tumor uptake [95, 96]. In the following sections, we will describe various NPs and their implications in detecting and/or treating PC.

i. Liposomes

Liposomes are synthesized from a phospholipid bilayer, assembled into a spherical vesicle with an aqueous core, enabling them to sheath both lipophilic and hydrophilic molecules [97, 98]. Liposomes are the simplest forms of vesicles among the organic NPs and they are famous as carriers for passive targeting [99]. By enhancing tumor uptake, these biodegradable and nontoxic liposomes were shown to promote the enhanced retention and permeability (EPR) effect at the tumor site [100, 101]. In addition, in a study conducted by Rajesh et al., curcumin loaded liposomes, with sizes ranging from 100-150 nm, and coated with anti-PSMA antibody, were used for drug delivery to PC cells. As determined by 3-(4,5-dimethylthiazol-2-yl)-2,5-diphenyl-2H-tetrazolium bromide (MTT) assay, treatment of the LNCap and C4-2B cell lines exhibited 70-80% loss in proliferation, while curcumin alone on the other hand, needed a 10x higher concentration to deploy the same cell killing effects [102]. Moreover, liposomes containing the molecular chaperone heat shock protein 90 (Hsp90) inhibitor 6BrCaQ for prostate adenocarcinomas were designed by Sauvage *et al.* Hsp90 demonstrates an essential role in the maturation of proteins involved in oncogenic pathways. Their results showed that the NPs induced apoptosis and cell cycle halt in PC3 cells while also synergizing with Doxorubicin (DOX) and slowing down cellular migration [103].

Regarding active targeting, Banerjee et al. synthesized liposomes for active targeting of DU-145 human prostate adenocarcinoma cell line. These liposomes were tagged to an anisamide ligand that targets sigma receptors and encapsulated Doxorubicin was used as the anti-malignancy agent. The anisamide-conjugated liposomal DOX (IC₅₀ 1.8 μM) showed extremely higher toxicity to DU-145 cells than non-targeted liposomal DOX (IC₅₀ 14 μM) [104].

However, a striking contradiction is revealed when exploring the literature on liposomes, since some studies have reported that they suffer from too many major weaknesses and defects such as easy oxidation, hydrolysis, and unstable structure. Also, these NPs are much less stable at elevated temperatures and some even experience high payload leakage. All in all, these setbacks resulted in their limited use as a vector for targeted transport and nano-therapy [105].

ii. Quantum Dots

Quantum Dots (QD) are semiconductor nanocrystals often synthesized from combinations of heavy metals such as Cadmium Selenite (CdSe), Cadmium Sulfide (CdS), Lead Sulfide (PbS) and Zinc Sulfide (ZnS) [106]. QDs have stolen the spotlight for a while because of their unique optical characteristics and various biomedical applications [107]. In addition, QDs exhibit great potential in various procedures such as cellular labelling, deep-tissue imaging, and as efficient fluorophores. In fact, traditional fluorescent labels fall short of providing long-term stability and concomitant detection of different signals when collocated to QDs.

On the other hand, PC applications concerning QDs are scarce with the major bulk addressing diagnosis and imaging rather than therapy [108-110]. Singh et. al., 2012, reported that CdS quantum dots instigated ROS-mediated apoptotic cell death in prostate malignant LNCaP cells, increase p53 and Bax protein expression [107]. Furthermore, Malekzad et. al., 2017, stipulated that the use of graphene quantum dots complexed with gold nanoparticles (GQDs/AuNP) and conjugated to anti-PSA antibodies, for dual signal amplification and highly sensitive PSA detection, was delineated [111].

Nevertheless, despite recent progressions, great concern has risen towards the heavy metal content of QDs. Depending on dosage and concentration, these metals can be potent toxins, neurotoxins, and teratogens, accumulating in and damaging the liver and nervous system [112]. Therefore, researchers have been instigated to pursue potentially safer alternatives such as silica-based Cornell dots

(C dots) [113]. These C dots are often coated with a neutral polymer such as polyethylene glycol (PEG), increasing their blood circulation by decreasing their renal clearance, while allowing them to be complexed to monoclonal antibodies enhancing their specificity and anti-cancer drug delivery potential [114].

iii. Gadolinium and Manganese NPs

To date, Gadolinium (Gd^{3+}) is famously employed as a contrast enhancing agent for magnetic resonance imaging (MRI) [115]. Areas with enriched Gd^{3+} are able to cross the blood brain barrier, exhibiting increased signal intensity, thus permeating brain tumors for ameliorated imaging [116, 117]. However, since Gd^{3+} is restricted to the extracellular environment, significant research efforts have focused on developing cell-permeable contrast agents [117]. In the case of Gd^{3+} , it can be loaded onto nanostructures, further increasing cellular uptake, and to acquire other properties such as specificity for targeted therapy [118]. In defense of the latter notion, Cui et. al., 2017 reported that bombesin (BBN) modified gadolinium oxide nanoprobe could enhance diagnosis and antitumor drug delivery in the future, by targeting over-expressed gastrin-releasing peptide (GRP) receptors in prostate adenocarcinomas [115].

Diversely, the use of manganese (Mn^{2+}) as a contrast agent in nanoprobe has just started to witness light. Little information was found to elucidate this topic, however, a study conducted by Gao et. al., 2012, reported the use of high-specificity Mn^{2+} doped ZnSe quantum dots for PC imaging with remarkable results achieved [119].

iv. Silver and Platinum NPs

Silver nanoparticles (AgNPs) are notorious as antimicrobial agents [120-122]. However, contrary to gold nanoparticles, AgNPs were seldom used against prostate adenocarcinomas. Scouring the literature on AgNPs' anti-tumor effects on prostate malignancy yielded few results. One study conducted by Mohammadzadeh, 2012, divulged that AgNPs possess the ability to bind to antioxidants in the prostatic tumor environment, thus allowing reactive oxygen species (ROS) to thrive, ultimately leading to the initiation of programmed cell death [123]. In support of the latter statement, a study by Firdhouse et. al., 2013 revealed that AgNPs induced PC3 apoptosis due to their cytotoxic effects. Notably, these effects were shown to be concentration dependent [124]. Finally, an *in vitro* study on AgNPs synthesized from the Chinese herbal plant *Cornus officinalis*, induced cytotoxicity to PC3 cells with a LC50 value of 25.54 µg/mL in 48 hours [125].

On the other hand, Wang *et al.*, 2013 developed mesoporous silica NPs hybridized with silver (Ag), for PSA detection in the human serum. The AgNPs demonstrated simplicity and enhanced sensitivity for PSA detection in contrast to conventional PSA detection techniques and assays including ELISA [126].

The role of Platinum-based NPs (PtNPs) in fighting PC lies primarily with regards to enhanced imaging and detection techniques [127, 128]. In one published article, Zhang et al., 2015, investigated the use of PtNPs conjugated to an anti-PSA antibody for a sensitive detection of PSA in the serum [129]. While Spain et al. took it a step further by proposing a refined method employing PtNPs complexed with a recombinant scFv antibody for the determination of PSA during PC diagnosis. These PtNPs were able to detect PSA at picomolar concentrations [130]. In the end, one interesting study by Taylor et. al., (2012) used superparamagnetic iron platinum nanoparticles (SIPPs) loaded with the chemotherapeutic drug paclitaxel and conjugated to an anti-PSMA antibody (J591) on prostate malignant cell line C4-2.

This resulted in a nano carrier with dual functions. The first being enhanced MRI contrast due to EPR, and the second being site-specific drug delivery in vivo by targeting PSMA [131].

v. Iron Oxide NPs

Iron oxide particles are often synthesized as superparamagnetic nanoparticles (SPIONs) having a diameter of 20 nm. These highly magnetic properties enable their use in several magnetic resonance technology-based biomedical applications. To prevent aggregation of the particles caused by van der Waals and hydrophobic interactions, and to mask these NPs from the immune system, polyethylene glycol (PEG) molecules are added to their surface [132]. Iron oxide nanoparticles are also coated with Silica to further enhance light absorption in imaging applications. Many studies using iron oxide particles against prostate adenocarcinomas exist in the literature [133]. However, one major project by Zhu and colleagues employed innovative iron oxide particles with significantly enhanced MRI and active targeting using PSMA receptors. Their SPIONs were able to infiltrate PSMA expressing malignant cells successfully and specifically, further strengthening the argument for their use as a theranostic approach for prostate adenocarcinomas [37].

At long last, Agemy et al. 2010 investigated the use of iron oxide nano-worms in prostate tumor blood vessels to induce nanoparticle-vascular-blockade in human PC. They aimed at obstructing tumor vasculature to induce necrosis. Their results demonstrated that conjugating the iron oxide nano-worms with a specific peptide that targets fibrin-fibronectin complexes result in the accumulation of the nanoparticles in the tumor vessels inducing additional local clotting; however, no significant inhibition of tumor growth was reported [134].

I. Gold Nanoparticles (AuNPs) Characteristics and use in Prostate Cancer

i. Characteristics

QDs, ceramic, metallic, oxide nanoparticles, and others are known to be difficult to disperse in fluid media. Their synthesis is thought to be challenging and the reaction is hard to control; eventually, consistency in their production is not constantly achieved. AuNPs on the other hand, have been greatly explored due to their ability to be directly synthesized in water, with great control over the particles size, shape and optical properties. They are also known for their generation simplicity, enhanced biodistribution and their potential to accommodate large payloads rendering them extremely appealing to scientists [135].

Moreover, AuNPs possess specific size and shape-dependent optical characteristics primarily concerning localized plasmon resonance [136]. When a light wave passes through the front, the surface electrons of the AuNPs become polarized and excited, thus causing them to oscillate in resonance with the frequency of the light [137]. Dynamic Light Absorption and scattering spectrophotometry highlight this phenomenon and they rely in concert on the metal and the surrounding, material size, shape and dielectric constants [138]. The highly sensitive surface plasmon resonance (SPR) response is crucial in order to measure any shift in the SPR that confirms any AuNPs modification caused by molecule attachment or size augmentation [139, 140].

ii. AuNPs for PSA detection

With regards to PSA detection in prostate adenocarcinomas, Rodriguez et al. (2018) delineated a porous silicon-based platform fastened to 100 nm gold nanoparticles (PSi-GNP), as biosensors for improved PSA detection, by enhancing conductivity in a sandwich bioassay [141]. A new method was described by Barbosa et al. (2017) towards achieving an optimized one-step quantitation of PSA with the use of silver enhanced AuNPs conjugated to anti-PSA antibodies in addition to carbon NPs [142]. PSA was successfully quantified in a relatively cheap, and effective method using the silver enhanced AuNPs, presenting a dynamic range of 10 to 100 ng/ml of PSA. On a similar note, Pal et al. (2017) used AuNPs braced with graphene oxide (Au-GrO) and tagged with anti-PSA antibodies as a novel biosensor applied to RWPE-1 human prostate epithelial cells. This fabricated NP sensor yielded a highly selective and stable model, with an extremely low PSA detection limit of 0.24 fg/mL [143]. In parallel, Suresh et al., (2018) applied an identical method for PSA detection however their AuNPs were coated with a chitosan layer to establish binding to the anti-PSA antibodies [144].

Additionally, Sattarahmady et al. (2017) described a round hairbrush-like gold nanostructure conjugated to an aptamer for PSA detection. The synthesized aptasensor was able to detect PSA with a minimal limiting value of 50 pg/mL [145]. Similarly, Srivastava et al. (2018) illumine a novel biosensor composed of graphene QDs and gold nanorods (GQDs-AuNRs). This nanocomposite was then coupled to either a conventional anti-PSA immunosensor, or an aptamer-based biosensor, to competently quantify and detect PSA levels. Both sensors ended up performing comparably, with a detection limit of 0.14ng/mL. However, the aptasensor nanocomplex did present some advantages over its competitor in terms of stability, simplicity, and cost effectiveness [146].

On the Other hand, Vural et al. (2018) outlined a self-assembled peptide nanotube (PNT), gold nanoparticle (AuNP) and polyaniline (PANI) composite (PANI/AuNP-PNT) for PSA detection in blood serum samples, used to alter a pencil graphite electrode (PGE). Anti-PSA Ab was immobilized on the modified electrode (PANI/AuNP-PNT/PGE) to snare PSA and horseradish peroxidase (HRP) labeled anti-PSA Ab was used as a tracer. The feasibility of the new technique was contrasted ELISA and well-matched results were obtained with a PSA detection limit of 0.68 ng/mL [147].

iii. AuNPs as active targeting theranostics

On the matter of actively targeting prostate adenocarcinomas using AuNPs, the floor is set for a study conducted in 2013 by Kasten et.al. The research team underlined the efficient feasibility of specifically targeting PC using PSMA inhibitor (CTT54)-homing gold nanoparticles. Compared to control non-targeted AuNPs, the PSMA-specific nanostructure demonstrated selective and higher binding capacity to LNCaP cells in a time-dependent manner [148]. Additionally, Shukla et al. (2012) overcame transport barriers for optimal payload delivery by employing functionalized radioactive gold nanoparticles (EGC-AuNPs) against tumor specific epigallocatechin-gallate (EGCG). Then the nanocomposite was coupled to a phytochemical extracted from green tea to target overexpressed laminin receptors on prostate adenocarcinoma cells and induce subsequent cytotoxicity [149].

Similarly, Tsai et. al. (2016) used a natural green tea extract EGCG on human PC-3 cells. In their study, the chemotherapeutic drug DOX was successfully conjugated to the EGCG-functionalized AuNPs to overcome the hurdles that accompany systemic anticancer drug delivery and conventional therapies, such as poor targeting and low intracellular uptake. MTT assays and Laser Scanning Microscopy results showed enhanced cellular uptake of DOX, accompanied by inhibited proliferation of the PC-3 cells [150].

A significant breakthrough emerged however, when Kim et al. (2017) succeeded in highlighting the selective uptake of epidermal growth factor-conjugated gold nanoparticle (EGF-GNP) and how it facilitates non-thermal plasma (NTP)-mediated cell death in prostate DU 145 cells along with other cell lines over-expressing the epidermal growth factor receptor (EGFR). Treatment with EGF-conjugated GNP complex, followed by NTP irradiation showed selective apoptosis of cells that underwent receptor mediated endocytosis. These results suggest that EGF-conjugated GNP functions as an important auxiliary endowing targeted specificity to applications of conventional plasma therapy [151].

Lastly, AuNPs were also extensively investigated as potential photothermal therapeutic (PTT) agents against PC. Due to their special optical properties and SPR, AuNPs are able to absorb light at the right frequency resulting in a hypothermic surrounding [152]. In support of these claims, Oh et al. (2015) employed PTT using AuNP clusters targeting PC3-cells. Low light irradiation applied on these nanoclusters caused local environmental heating, thus selectively killing targeted malignant PC3 cells [153].

iv. AuNPs as Imaging Enhancers

Since AuNPs possess inert qualities, they were also investigated as powerful imaging enhancers for PC. Furthermore, AuNPs were shown to outshine other fluorophores by having superior emission spectra by 4 to 5 folds [154]. In a study conducted by Harmsen et al., 2017, 60 nm gold nanoparticles were encapsulated with a silica shell to achieve an optimistic contrast agent for in vivo malignancy imaging. The research team described various applications of these nanoprobe for biomedical research such as intraoperative cancer photography and an elementary depiction of prostate malignancy without the need for specific targeting biomarkers [155]. X-rays, CT scans, photoacoustic imaging, ultrasounds, and others, all are imaging procedure that are ameliorated with the use of AuNPs [156].

J. Dendritic Poly-L-Lysine: Importance and role

Dendrimers are highly branched, monodisperse, and symmetrical macromolecules of nano-size dimensions consisting of a central core, branching units, and terminal functional groups [157, 158]. This structure encourages the creation of nanocavities, the environment of which dictates the solubilizing or encapsulating capabilities of dendrimers, whilst the exterior groups essentially define their chemical activity, including targeting capabilities. Hyperbranched polymers, on the other hand [159, 160], are branched polymers with nanocavities, but unlike dendrimers, they are nonsymmetric and polydispersed. The latter polymers, on the other hand, are easier to make and thus less expensive than dendrimers, which need time-consuming multistep reaction methods. Furthermore, unlike dendrimers, which are made from conventional monomers, dendrigraft polymers [161, 162] are made from reactive oligomers or polymers by a series of protect-deprotect grafting procedures. By analogy with dendrimers, each grafting step is referred to as a generation [163]. Dendrigrafts, in contrast to dendrimers, have bigger structures, grow considerably faster, and amplify surface groups more intensely as a function of generational development. Dendritic polymers include dendrimeric, hyperbranched, and dendrigraft polymers, all of which have an accumulation of functional groups on their exterior surface as a common feature. Dendritic polymers' exterior groups can be changed, resulting in a variety of functional materials that can be used in a variety of applications, including drug administration. In this regard, the majority of commercially available or custom-made dendritic polymers have been functionalized adequately for use as drug delivery vehicles, [164, 165] as gene delivery vectors [166, 167] or as drugs on their own [168].

Among the impressive number of dendritic polymers reported in the literature thus far, the poly(amine)-based ones, which include the well-known poly(amidoamine) and poly(L-Lysine) dendrimers, as well as poly(L-lysine) polymers and linear poly(L-Lysine) polymers, and the hyperbranched poly(ethylenimine) polymers have undoubtedly piqued the interest of the chemical biology community. Denkewalter et al. described poly-L-lysine dendrons for the first time in a patent before the introduction of poly(amine)-based polymers, [169, 170], and they were quickly exploited for the manufacture of synthetic vaccines during the 1980s [171]. At physiological pH, the polycationic character of these poly(amine)-based polymers is suitable for cellular adhesion, endocytosis, and intracellular trafficking for medicinal delivery, genetic material transfection, or imaging in cellulosic materials [172]. However, due to their cytotoxicity and non-degradability, low synthetic availability, non-sustainable synthesis, high dispersities, and batch-to-batch variation, these abiotic macromolecules exhibit some undesirable characteristics, [173-175] highlighting the need for a new generation of dendritic polymers that overcome those major drawbacks for real-world bio-applications [176]. Furthermore, four distinct generations of d-PLL can be obtained via the slow hydrolysis of the side chain-protected building block Lys(Tfa)-NCA, and figure 18 (retrieved from <https://hal.archives-ouvertes.fr/hal-01814843> by Françoise Jean-Patrick, 2018) neatly illustrates the reaction process [177].

Finally, in a study conducted by Tsogas et al., 2007 Two generations of poly(L-lysine) dendrigrafts (DGLs) were investigated, and their internalization profiles examined in A549 human lung carcinoma cells. Their evidence revealed that DGLs of the third generation are extremely toxic, making them unsuitable for use as medication or gene delivery vehicles. In contrast, their second-generation equivalents are rather benign, and these derivatives, particularly the guanidinylated derivatives, are interesting candidates for medication and gene delivery due to their biodegradable nature [178].

K. Importance of siRNA and Folate Receptors in Prostate Cancer

Progressions in the genetic nature of diseases including cancer have helped illuminate target genes associated with disease advancement. The discovery of small RNA interference effectors, namely siRNA, that were able to selectively downregulate specific genes, paved the way for developing RNA-based treatments [17, 179]. In the following section, five of the most recent studies employing siRNA-based therapeutics in prostate cancer will be discussed. Starting with Cornelius et al., 2021, where Ero 1 α (chief regulator of oxidative folding and redox homeostasis) knockdown was achieved via siRNA transfection in PC cell lines. In fact, Ero 1 α silencing was proven to dysregulate levels of integrin β 1 in PC3 cells, while inhibiting their proliferation, migration, and invasion [180].

On the other hand, Liu Wei et al., 2021 claim that pre-mRNA processing factor 6 (PRPF6) act as a primary modulator of androgen receptors in PC and silencing it via targeted siRNA sequences (directly or through Lentivirus transfection), reduces tumor growth in PC cell lines while significantly suppressing xenograft tumors even under castration conditions *in-vivo*, using a murine model [181]. Additionally, Han Q. et al, 2021 recently demonstrated an efficient method to silence SIRT6 by aptamer-modified exosomes carrying siRNA. They also elaborated on the fact that silencing SIRT6 by siRNA inhibited tumor growth and metastasis in PC xenograft mice models.

However, to facilitate the translation of siRNA therapeutics into the medical field, the use of safe, effective, and non-cytotoxic cargo delivery systems is a prerequisite. Fortunately, the elaboration on novel biomaterials has facilitated the synthesis and bioactivation of various multifunctional NPs to deliver siRNA. Some of these have been reported in the treatment of both solid tumors and blood-borne malignancies [182-184]. Recently, stem cell membrane camouflaged polydopamine carrying DOX and

programmed cell death ligand 1 (PD-L1) siRNA NPs (PDA–DOX/siPD-L1@SCM) were synthesized and used by Mu Xupeng et al., 2021, as a targeted chemoimmunotherapeutic agent against PC metastasis to the bone. In their study, PDA–DOX/siPD-L1@SCM NPs exhibit excellent synergistic chemoimmunotherapeutic effects, as PD-L1 siRNA downregulates PD-L1 on tumor cells, thus restoring T cell anti-tumor properties, while DOX induces tumor cells death [185].

In addition, Oner Ezgi et al., 2021 employed a cationic solid lipid nanoparticle/siRNA complex targeting EphA2 receptor (cSLN/siEphA2 complex) as a treatment for advanced PC *in-vitro* with high levels of EphA2 expression. They discovered that cSLN/siEphA2 alone could not affect PC3 cell viability, migration, nor proliferation. However, in combination with a histone lysine demethylase pan-KDM inhibitor JIB-04, these results were easily achievable with high transfection efficiency [186].

On a different note, PSMA expression and PC progression are directly proportional [187, 188]. This provided an excellent target for the treatment of the disease, mainly in its more advanced and metastatic forms [74, 189]. High levels of PSMA have also been found on PC metastasis however, no significant measurements were detected in healthy tissues, rendering it as an attractive target for treating metastatic PC [82, 190]. PSMA exhibits a duality in its enzymatic function. It acts as a glutamate carboxypeptidase and folate hydrolase that cleaves the amide bond of *N*-acetyl aspartyl glutamate and hydrolyzes extracellular polyglutamated folate to mono-glutamic folic acid that is subsequently used by PC cells [188]. In addition, it has been postulated that overexpression of PSMA might provide PC cells with a survival advantage, further implicating PSMA in the metabolism of polyglutamated folates and the subsequent uptake of folates [190, 191]. Folic acid (FA), a high affinity ligand for the folate receptor (FR), keeps its receptor binding and endocytosis properties when covalently attached to a multitude of molecules and nanoparticles [192-194]. Therefore, folate-conjugated nanoparticles could be used as PSMA-targeted nanocarriers for the delivery of a therapeutic agent to PSMA-positive PC cells [195].

Indeed, this work mainly focuses on studying the effect of increasing concentrations of reaction components (polymer, salt precursor, and reducing agent) on AuNPs size, the synthesis, and characterization of AuNPs as potential cargo delivery vehicles against PC. Furthermore, we aimed at functionalizing our carriers via the use of FA as a targeting agent in a PSMA-positive PC cell line. Additionally, the ability of our vectors to completely complex siRNA was investigated using a green fluorescent Universal Negative Control #1, 6-FAM siRNA. This also allowed us to assess the binding capacity of our targeted nanocomposite against PSMA, and to visualize the internalization of our carrier *in-vitro*.

III. Materials and Methods

Chemicals

Purified H₂O (resistivity » 18.2 MΩ cm) was used as a solvent. Glassware was cleaned with aqua regia (3 parts of concentrated HCl and 1 part of concentrated HNO₃), rinsed with distilled water, ethanol, and acetone and oven-dried before use. Tetrachloroauric acid trihydrate (HAuCl₄, 3H₂O), L-Ascorbic Acid, Phosphate Buffer Saline (PBS), and MISSION® siRNA Fluorescent Universal Negative Control #1, 6-FAM were purchased from Sigma Aldrich. Thiol terminated poly (ethylene glycol) methyl ether, M_w = 5400, was purchased from Polymer Source. Poly (L-lysine) dendrigraft (PLL) with an average molecular weight of 7 KDa was synthesized and characterized by a previously reported method [20]. All chemicals were used as received, without further purification or modification.

Cells and Culture Conditions

PC-3 PSMA positive cell lines were kindly provided by Prof. Giulio Fraccasso (University of Verona, Italy). Cell lines were cultured in RPMI 1640 (Sigma- Aldrich) complemented with 10% fetal bovine serum and antibiotics (100 U/mL penicillin and 100 µg/mL streptomycin) in a humidified atmosphere with 5% CO₂ at 37°C. Cells were grown in a monolayer (70–80% confluency), before being transfected with coated gold nanoparticles (AuNPs), such as siRNA.AuNPs-d-PLL-PEG-OCH₃ and siRNA.AuNPs-d-PLL-PEG-FA

siRNA Transfection

Small interfering RNA (siRNA) used in this study was MISSION® siRNA Fluorescent Universal Negative Control #1, 6-FAM (lyophilized). siRNA was dissolved in 1mL sterile DNase/RNase free water, according to the manufacturer's instructions (Sigma-Aldrich). Cells were starved in serum free media, then directly transfected for the designated times with siRNA (25 and 50 nM), coupled with AuNPs-d-PLL-PEG-OCH₃ and AuNPs-d-PLL-PEG-FA as transfection vectors.

Synthesis of Charged, d-PLL-Coated Gold (Au) Nanoparticles Under Various Conditions

A. **Effect of Increasing HAuCl₄ Concentration (0.125 mM to 1 mM):** Four 50 mL round bottom flasks each containing 0.750 mL d-PLL (200 μ M) were prepared as follows: flask one containing 23.9 mL dH₂O, and 0.168 mL HAuCl₄ (13 mM). Flask two with 23.726 mL dH₂O, and 0.336 mL HAuCl₄ (13 mM). Flask three contained 23.390 mL dH₂O, and 0.672 mL HAuCl₄ (13 mM). Flask four having 22.718 mL dH₂O, and 1.344 mL HAuCl₄ (13 mM). Finally, 0.187 mL of Asc Ac (0.1 M) were rapidly injected into each of the four flasks to initiate the reactions. All flasks were kept at room temperature with constant stirring, d-PLL was used for coating, and L-ascorbic acid (Asc Ac) was used a reducing agent. The reactions were left overnight to achieve completion.

B. **Effect of Increasing d-PLL Concentration (1 μ M to 12 μ M):** Similarly, four 50 mL round bottom flasks each containing 0.336 mL HAuCl₄ (13 mM) were prepared as follows: flask one contained 0.125 mL d-PLL (200 μ M) in 24.351 mL dH₂O. Flask two had 0.375 mL d-PLL (200 μ M) in 24.101 mL dH₂O. Flask three containing 0.750 mL d-PLL (200 μ M) in dH₂O. Flask four having 1.5 mL (200 μ M) d-PLL in 22.976 mL dH₂O. Finally, 0.187 mL of Asc Ac (0.1 M) were rapidly injected into each of the four flasks to initiate the reactions. All flasks were kept at room temperature with constant stirring. The reactions were left overnight to achieve completion.

C. **Effect of Increasing Asc Ac Concentration (ex 1 to ex 5):** For this set of reactions, four 50 mL round bottom flasks each containing 0.336 mL HAuCl₄ (13 mM) and 0.750 mL d-PLL (200 μ M) in four different volumes of dH₂O (23.851 mL, 23.817 mL, 23.726 mL, and 23.601 mL respectively). Finally, each flask was rapidly injected with 0.0625 mL, 0.097 mL, 0.1875 mL, and 0.3125 mL 0.1M Asc Ac to initiate the syntheses. All flasks were kept at room temperature with constant stirring. The reactions were left overnight to achieve completion.

Synthesis and Characterization of AuNPs for siRNA Delivery

A. **Synthesis of AuNPs-d-PLL:** In a 50 mL round flask containing 22.07 mL of deionized water, 1.440 mL HAuCl₄ (13 mM) was added under stirring, followed by the quick addition of 1.250 mL of d-PLL (200 μM) as coating ligand and 0.250 mL of ascorbic acid (0.1 M) as a reducing agent. Upon the addition of ascorbic acid, the color of the solution changed from pale yellow to blue reddish/brown. The solution was kept under stirring overnight. The obtained nanoparticles had a hydrodynamic diameter of about 118.8 ± 1 (Z avg) and a zeta potential $+32 \pm 1.3$ mV.

B. **B. Synthesis of AuNPs-PEG by PEGylation of AuNPs-d-PLL:** To 5 mL of AuNPs-d-PLL colloidal solution under stirring, 0.27 mL of SH-PEG 5000 (185 μM) was added dropwise for 5 minutes, the solution was kept under stirring for two hours. The successful PEGylation was confirmed by DLS. The size of AuNPs-d-PLL was found to increase from 118.8 ± 1 (Z avg) to 133.1 ± 0.9 nm (Z avg) while the zeta potential was found to decrease from $+32 \pm 1.3$ mV to $+21 \pm 1$ mV confirming the attachment of PEG onto AuNPs-d-PLL surface (AuNPs-d-PLL-PEG). Furthermore, AuNPs-d-PLL-PEG-FA possessed a hydrodynamic diameter of 125.5 ± 5 nm (Z avg) and a zeta potential of $+30 \pm 0.9$ mV.

Dynamic Light Scattering and Zeta Potential measurements

The size distribution and surface charge (zeta potential) of AuNPs colloidal solutions were determined by dynamic light scattering (DLS) with the Malvern Zetasizer Nano-ZS (model ZEN3600; Malvern, Worcestershire, WR14 1XZ, UK) using the default NIBS 173° back scatter technique. The model used in the fitting procedure was based on Mark Houwisk parameters. Data was fitted using the cumulative fit given by the suppliers. Measurements were performed on the pristine solutions of AuNPs

(~50 µg/mL) using disposable folded capillary cuvettes at 25 °C. Triplicates of each sample have been made for result comparison efficiency.

Uv-Vis Spectrophotometry of AuNPs-d-PLL and AuNPs-PEG

0.5 mL of each of our previously synthesized AuNPs-d-PLL were withdrawn and injected into black quartz cuvettes each, for Uv-Vis spectrophotometry. Purified H₂O was used as blank, and readings were performed in triplicates using UV-Vis Analytikjena SPECORD[®] 250 PLUS spectrophotometer (300–900-nm range, 0.5 nm resolution). Finally, obtained spectra were plotted on EXCEL for further analysis.

WST-1 Cell Proliferation Assay

PC-3-PSMA cells at log phase were seeded in a 96-well plate at a seeding density of 5×10^4 cells/mL and incubated overnight. Cells were treated with 50 µg/mL of AuNPs-d-PLL-PEG-FA for four, six, eight, 12 and 24 hours. As a control, AuNPs were resuspended with deionized water and serum free media to reach the tested concentration in a final volume of 500 µL, of which 200 µL were loaded into the respective wells. After each timepoint was reached, the cells were washed with 1x sterile PBS, and then incubated with 10 µL of WST 1 reagent in serum free media (Durocher I. et al., 2017) for 2 hours. Results were read at 450 nm using the Thermofisher MultiGo-Scan ELISA reader.

Gel Electrophoresis

In 200 µL DNase/RNase free PCR tubes, siRNA:AuNPs with three sorts of mass to ratio (MR) concentrations were prepared; MR 10, 20 and 30. siRNA concentration was set at 0.25 µg/mL for all samples. For MR 10, 2 µL siRNA (13.8 µg) were added to 5.52 AuNPs and 11.04 µL RNase free water. For MR 20, 2 µL siRNA (13.8 µg) followed by 11.04 µL AuNPs and 5.52 µL RNase free water were added. For MR 30, 2 µL siRNA (13.8 µg) were mixed to 16.56 µL AuNPs. All samples were

kept in the dark at RT for 1hr with constant low shaking, followed by the addition of 2 μ L loading buffer. Eventually, samples were loaded on a previously prepared 1.5% Agarose gel and left to run at 100 mV for 30 mins. The obtained gel was photographed under UV light using ChemiDoc™ and the band intensity was analyzed for comparison.

Flow Cytometry

PC3-PSMA cells were seeded at 100,000 cells per well in a flat bottom adherent 24-well plate ($n = 3$) and cultured for 24hrs following normal growth conditions (RPMI, 5% CO₂, 37° C). Cells were then incubated with 100 μ L of 25 and 50 nM fluorescent siRNA complexed with AuNPs-d-PLL-PEG MR 25 (500 μ g/mL) and AuNPs-d-PLL-PEG-FA MR 25 (500 μ g/mL) and incubated for 24hrs in 300 μ L normal growth medium (RPMI + 10% FBS + 0.1% PS). Cells were then washed twice with culture grade 1x PBS, then trypsinized. Collected cells were centrifuged at 1000 rpm for 5 mins and resuspended in 1mL cold FACS Buffer (3% PFA + 0.2% BSA, in 1x PBS). Gates were set at 50,000 cells per sample, and siRNA-FITC fluorescence was detected using a Partec Cube 8 Flow Cytometer and analyzed using FlowJo.

Fluorescence Microscopical Analysis of siRNA-NPs Localization

PC3-PSMA cells were seeded at 1×10^6 cells per well in a flat bottom adherent 6-well plate and incubated for 24hrs following normal growth conditions (RPMI, 5% CO₂, 37° C). Cells were then transfected with 100 μ L of 25 and 50 nM fluorescent siRNA complexed with AuNPs-d-PLL-PEG MR 25 (500 μ g/mL) and AuNPs-d-PLL-PEG-FA MR 25 (500 μ g/mL) and incubated for 4 hrs in 500 μ L serum free RPMI. Cells were then washed twice with culture grade 1x PBS and fixed with 4% PFA for 10 mins at room temperature in the dark. Following fixation, cells were washed again with 1x PBS and incubated with 1% Triton X 100 in PBS for 5 mins. Cells were then blocked for 30 mins using a solution

of PBS-Tween 20, BSA and Tris pH 8.8. After blocking, cells were washed and incubated with monoclonal rabbit anti- Early Endosomal Marker (EPR4245; dilution 1:100; Alexa Fluor® 647, Abcam, Cambridge CB2 0AX, UK) and rabbit monoclonal anti- Lysosome Membrane Marker (EPR6599; dilution 1:150; Alexa Fluor® 594 Abcam, Cambridge CB2 0AX, UK). Prior to the mounting medium, nuclear fragmentation was tracked with 100 µL Hoechst S769121 (1.5 µg/ml; Abcam, Cambridge CB2 0AX, UK) at 4°C for 1 hr. Images were obtained by laser scanning confocal microscopy, Zeiss LSM 700. For Hoechst, UV- light with blue filter was used. As for the fluorophore conjugated antibodies, pseudo-green and red dual excitation light was used and split to obtain separate images.

Testing Intracellular Localization Using Z-stacks

Z-stack slicing was performed on representative samples of AuNPs-d-PLL-PEG.siRNA 50nM and AuNPs-d-PLL-FA.siRNA 50 nM. Laser gains were set at 600 nm for Alexa Fluor 488, EEA-1 and M6RP, and 500 nm for Hoechst stain. In total, 20 sections were captured with a range of 10 µm and an interval of 1 frame/second. The smallest section was set at 2.73 µm (default) and all lasers had matched pinholes.

Statistical Analysis

The data are reported as means ± SEM and were analyzed by one-way ANOVA. The differences between experimental and control groups were assessed by post-hoc and Tukey's test. Statistical significance was recognized at $p < 0.05$ and each experiment was conducted and validated at least three times. Significance was reported on each graph with * representing a p value < 0.05 , ** representing a p value < 0.01 , and *** representing a p value < 0.001 . NS corresponds to non-significant difference.

Ethics Statement

The study is in compliance with the recognized international standards and principles of the Declaration of Helsinki, and has received ethical approval from the institutional review board (IRB) at Notre Dame University - Louaize with the following reference number (CNRS #GRP2017).

IV. Results

Characterization of Charged, d-PLL-Coated Gold (Au) Nanoparticles under Various Conditions

Post synthesis, AuNP colloidal solutions were cooled down to room temperature for two hours. The size and charge of AuNPs-d-PLL synthesized under various experimental conditions were analyzed using Dynamic Light Scattering and ZETA measurements. Prior to any readings, all NPs were diluted to the lowest sample concentration of each set. All measurements were conducted using folded capillary tubes and in triplicates to ensure reproducibility. AuNPs-d-PLL synthesized with 0.125 mM HAuCl₄ presented a hydrodynamic diameter of 50.45 ± 0.28 nm (Z avg), which increased following the increase in HAuCl₄ concentration, reaching a size of 69.49 ± 0.77 nm for AuNPs at 0.25 mM HAuCl₄ (table 1). This increase in size was also reported for particles synthesized at 0.5 mM HAuCl₄, as their size reached a Z avg of 90.82 ± 2.81 nm. Finally, AuNPs-d-PLL synthesized using 1 mM HAuCl₄ presented the largest increase in Z avg (35 nm, compared to NPs at 0.5 mM), and had a hydrodynamic diameter of 125.0 ± 2.6 nm (table 1, figure 1). With regards to surface charge, all synthesized particles were stable with a ZETA potential higher than (+) 21 mV. In fact, the lowest recorded surface charge belonged to AuNPs-d-PLL synthesized at 0.125 mM HAuCl₄ ((+) 23.3 ± 4.1 mV) (table 1). The ZETA potential of the particles steadily increased with increased HAuCl₄ concentrations, reaching (+) 25 ± 0.6 mV for particles synthesized at 0.25 mM HAuCl₄, followed by (+) 31.4 ± 1.4 mV for particles synthesized at 0.5 mM, and finally, the highest ZETA potential was recorded at (+) 40.8 ± 1.2 mV for particles synthesized using 1 mM HAuCl₄ (table 1, figure 2).

Increasing the concentration of d-PLL increased the size of nanoparticles only slightly. The size increased from about 66 nm to about 82 nm when the concentration of d-PLL increased from 1 μ M to 12 μ M (table 1, figure 2). To further understand the effect of d-PLL concentration on the size of our AuNPs, data concerning Size Intensity (extracted from DLS) was plotted as a function of d-PLL concentration using EXCEL (table 1; figure 2, Panel C). A positive ascending trend is observed. As the

concentration of d-PLL increased, the size intensity of our NPs increased. However, this ascending trend proved non-significant. Particles synthesized using 1 μM d-PLL had a size intensity of 82.29 ± 1.11 nm, followed by AuNPs-d-PLL 3 μM at 83.38 ± 1.63 nm, AuNPs-d-PLL 6 μM at 87.54 ± 3.97 nm, and AuNPs-d-PLL 12 μM at 99.43 ± 1.97 nm. In terms of ZETA potential, no clear effect of d-PLL was noticed on the surface charge of the particles. However, all synthesized particles were stable with a Zeta potential greater than (+) 30 mV. The lowest recorded charge belonged to AuNPs-d-PLL 6 μM at (+) 32.9 ± 1.1 mV, followed by AuNPs-d-PLL 3 μM at (+) 35.5 ± 1.1 mV, AuNPs-d-PLL 12 μM at (+) 36.6 ± 2.5 mV, and lastly, AuNPs-d-PLL 1 μM at (+) 37.5 ± 0.9 mV.

Lastly, studying the effect of increasing Asc Ac revealed that particles synthesized using ex 1 Asc Ac had an average size of 89.92 ± 2.05 nm. Interestingly, upon using an excess of 1.55 Asc Ac, the size of AuNPs-d-PLL decreased reaching 80.31 ± 2.41 nm (table 1, figure 3). Similarly, upon further increasing Asc Ac to ex 3, the Z avg of the NPs decreased reaching 74.03 ± 1.32 nm. However, the most noticeable decrease in Z avg was for AuNPs-d-PLL synthesized using ex 5 Asc Ac possessing a Z avg of 64.65 ± 0.42 nm. In terms of the ZETA potential of these particles, no significant effect of increasing Asc Ac concentration was noticed. However, all synthesized particles were stable with a ZETA potential greater than (+) 25 mV, and an average surface charge of (+) 30 ± 2 mV.

In addition to DLS-ZETA measurements, Uv-Vis spectroscopy was performed on all AuNPs in triplicates as well. Similarly, all AuNP solutions were diluted to the lowest sample concentration prior to the analysis, and black quartz cuvettes were used to perform the readings. Lastly, all readings were performed in triplicates. Particles synthesized using 0.125 mM HAuCl₄ had a maximum absorbance of 0.5468 at 543 nm (table 1). A red shift on 8 nm was noted when increasing HAuCl₄ to 0.25 mM (0.5431 at 551 nm) (table 1, figure 10). This shift became even more prominent with AuNPs 0.5 mM-d-PLL (0.5624 at 571 nm, 21 nm). Furthermore, AuNPs 1 mM-d-PLL presented an even larger shift to the right

(31 nm) having a maximum absorbance of 0.2847 at 602 nm (table 1, figure 10). Concerning the effect of d-PLL concentration on AuNPs size, particles synthesized with 1 μ M d-PLL had a peak absorbance of 1.1413 at 570 nm. A small shift to the right of 1 nm was noticed when d-PLL concentration was increased to 3 μ M (1.1426 at 571 nm) (table 1, figure 11). This red shift further increased to the right by a value of 9 nm with AuNPs-d-PLL 6 μ M. The largest red shift was recorded for AuNPs-d-PLL 12 μ M (26 nm) having a peak absorbance of 1.0221 at 597 nm (table 1, figure 11). Finally, with respect to increasing Asc Ac concentration on particle size, AuNPs-d-PLL-Asc Ac ex 1 exhibited the widest peak absorbance of 1.0757 at 595 nm (table 1, figure 12). Interestingly, a shift to the left (22 nm) is noted with AuNPs-d-PLL-Asc Ac ex 1.55. This phenomenon was also witnessed with AuNPs-d-PLL synthesized with excess 3 Asc Ac, as their absorbance peaked at 1.0799 at 566 nm (blue shift 7 nm). As expected, the largest blue shift (compared to ex 1 NPs) was recorded for AuNPs-d-PLL-Asc Ac ex 5, with a maximum absorbance of 1.1174 at 554 nm (table 1, figure 12).

Characterization of AuNPs-d-PLL for siRNA Delivery

As previously stated, DLS-ZETA measurements, and Uv-Vis spectroscopy were performed in triplicates to ensure reproducibility of the results. AuNPs-d-PLL presented a hydrodynamic diameter of 118.8 ± 1 nm (Z avg), which increased following the slow addition of FA reaching a size of 125.5 ± 5 nm for AuNPs-d-PLL-PEG-FA (table 2). AuNPs-d-PLL-PEG-OCH₃ registered the largest diameter of 133.1 ± 0.9 nm (Z avg) when compared to the previously mentioned particles (figure 7). On the other hand, with regards to the surface charge of AuNPs, AuNPs-d-PLL presented a positive charge of $(+) 32 \pm 1.3$ mV, which gradually decreased upon addition of PEG and FA, reaching $(+) 30.2 \pm 0.9$ in the case of AuNPs-d-PLL-PEG-FA, and $(+) 21 \pm 1$ mV for AuNPs-d-PLL-PEG-OCH₃ (table 2, figure 8).

UV-vis analysis revealed that AuNPs-d-PLL possessed a peak absorbance of 0.5183 at 572 nm. A red shift of 4 nm was noted for AuNPs-d-PLL-PEG-FA, having a peak absorbance of 0.5156 at 576

nm. Finally, AuNPs-d-PLL-PEG-OCH₃ exhibited the largest red shift of 6 nm (compared to AuNPs-d-PLL) with their absorbance peaking at 0.5647 at 578 nm (table 2, figure 9).

Following AuNPs-d-PLL synthesis, the particles were then complexed with two concentrations of siRNA (25 and 50 nM), while maintaining a constant MR of AuNPs.siRNA, at MR 25, throughout all samples. For particles subjected to 25 nM siRNA, AuNPs-d-PLL.siRNA demonstrated an increase in hydrodynamic diameter reaching 123.5 ± 2.2 (Z avg), as seen in table 2. Furthermore, AuNPs-d-PLL-PEG.siRNA exhibited a Z avg of 135 ± 4 nm, followed by the largest particles, AuNPs-d-PLL-FA.siRNA with an average size of 193.5 ± 1.9 nm (table 2). However, the greatest change was observed when measuring AuNPs surface charge upon the addition of the very negatively charged siRNA. AuNPs-d-PLL.siRNA 25 nM witnessed a decrease in ZETA potential from (+) 32 ± 1.3 mV to (-) 21.13 ± 0.5 mV, followed by AuNPs-d-PLL-PEG.siRNA 25 nM, with a charge of (-) 14.13 ± 4.87 mV, and finally, for AuNPs-d-PLL-FA.siRNA 25 nM, the surface charge decreased from (+) 30.2 ± 0.9 mV and reaching (-) 11.41 ± 3.78 mV (table 1). Subsequently, for particles subjected to 50 nM siRNA, the same analysis was performed with similar results (table 2). As seen in figure 3, particles witnessed an increase in their average size, with AuNPs-d-PLL.siRNA 50 nM becoming the largest (Z avg 139.6 ± 1.3 nm), followed by AuNPs-d-PLL-FA.siRNA 50 nM (Z avg of 136 ± 1.5 nm), and finally, AuNPs-d-PLL-PEG.siRNA 50 nM being the smallest of the particles with an average diameter of 134 ± 1 nm. Lastly, particles also exhibited noticeable change in ZETA potential. AuNPs-d-PLL.siRNA 50 nM became strongly negative with a surface charge of (-) 23.6 ± 2 mV, followed by AuNPs-d-PLL-FA.siRNA 50 nM with a ZETA potential of (-) 11.5 ± 1.5 mV, and finally AuNPs-d-PLL-PEG.siRNA 50 nM having a surface charge of (-) 4.4 ± 1.4 mV (table 2).

WST-1 Cell Proliferation Assay

To investigate the effect on cellular proliferation of our AuNPs-d-PLL on PC3-PSMA cells, a WST-1 reagent was used. The tetrazolium salt, WST-1, is cleaved by a cellular mechanism that occurs mainly at the cell surface (Guertler, A., et al., 2011) forming soluble formazan. This reduction is highly dependent on the glycolytic production of NAD(P)H in viable cells. The data reported in figure 13 support the non-cytotoxic effects of AuNPs-d-PLL since the percent viability remained above 80 % for all the time points. Even after a 24-hour incubation period, percent viability remained satisfactory with 80.15% viability as compared to the control.

siRNA complexation of differently coated AuNPs (PLL, PEG, FA)

In order to visualize the effect of siRNA addition on our NPs, siRNA complexation was performed *in-situ*, on a 1.5% Agarose gel. AuNPs-d-PLL.siRNA complexation initiated at MR 10, with slight decrease in band intensity at MR 20, followed by complete band disappearance at MR 30, marking total AuNPs-d-PLL.siRNA complexation (Figure 14). On the other hand, AuNP-d-PLL-PEG OCH₃.siRNA complexation at MR 10 was less evident when compared to AuNPs-d-PLL.siRNA, with a similar decrease in band intensity at MR 20 (figure 14, panels A and B). Similarly, complete complexation was achieved at MR 30. Finally, AuNP-d-PLL-PEG FA.siRNA complexation in panel C was less noticeable at MR 10 when compared to NPs in panels A and B. However, comparably to NPs from panels A, and B, complexation became prominent at MR 20, and finalized at MR 30. This indicates that complete siRNA complexation was achieved between MR20 and MR30 irrespective of the coating agent used on our AuNPs. Lastly, positively charged AuNPs-d-PLL ((+) 32 ± 1.3 mV) showed earliest signs of siRNA complexation with faintest band intensity at MR 10 (figure 14, panel A).

Binding ability of various AuNP complexes by flow cytometry

Counts of fluorescently labeled siRNA-PSMA were compared among different doses and types of NPs as illustrated in figure 15. With regards to side scattering, no significant change was observed among the samples (panel A). Therefore, a quantification of cells containing FITC-labeled-siRNA was performed. The method used was adopted from Shin et al 2020, where the percentage of cells containing FITC siRNA was calculated from cells with higher FITC signals than the threshold (Shin, H., et al., 2020). The threshold value was calculated from the median + robust SD (retrieved from FlowJo) of the control, untreated samples (panel B). This allowed for statistically meaningful measurements. Then, the data was extracted and plotted using EXCEL (panel C).

In terms of fluorescence, a non-remarkable fluorescent FL-1 intensity corresponding to FITC siRNA signal was observed for naked siRNA and AuNPs-d-PLL-PEG.siRNA (Figure 15, C). On the other hand, increased FL-1 fluorescence was marked for 25 and 50 nM AuNPs-d-PLL-PEG-FA.siRNA that is quite significant compared to naked siRNA-NPs (~ 17%, and ~ 30%, respectively). As depicted in the bar graph, the highest mean fluorescence peaked with AuNPs-d-PLL-PEG-FA.siRNA at 50 nM concentration compared to the low FL-1 levels of PSMA-siRNA lacking NPs. Interestingly, untreated PSMA-PC3 cells showed background levels similar to PSMA-siRNA at 25nm. Moreover, AuNPs-d-PLL-PEG at both 25 and 50 nM siRNA did not show any significant difference of fluorescence with respect to control samples and to cells incubated with AuNPs-d-PLL-PEG-FA.

Uptake of fluorescein-siRNA conjugated NPs in PC3-PSMA cells

To decipher the exact subcellular localization of AuNPs-d-PLL-PEG-FA.siRNA 50 nM, cells were fixed and stained with Hoechst, early endosomal marker (EEA1), or lysosomal marker (M6PR) post-incubation with the NP complexes for 4 hrs at 37 °C. Using AuNPs-d-PLL-PEG-FA.siRNA 50 nM was again marked as dot-like structures dispersed in the cytoplasm, with remarkable perinuclear

presence (Figure 16, D and E, pseudo-green panels). Next, to determine the uptake pathway, we ought at merging siRNA stain with EEA1 and M6PR stains. Interestingly, almost 30% of cells showed slight yellow zones indicating co-stains with the endosomal marker (Figure 16, D and E, overlay). This overlap was only remarkable in cells treated with AuNPs-FA.siRNA and was absent in PSMA cells treated with AuNPs-d-PLL-PEG.siRNA 50 nM (Figure 16, B and C, overlay).

Finally, as a last resort to confirm AuNPs internalization, Z-stack imaging was performed. Samples with AuNPs-d-PLL-PEG-FA.siRNA 50 nM and AuNPs-d-PLL-PEG.siRNA 50 nM were selected for a series of twenty consecutive images captured at focal distances ranging from $-10\ \mu\text{m}$ to $+10\ \mu\text{m}$. A set of eight images was chosen as a representative for both AuNPs-siRNA-FA 50 nM (figure 17, panel A) and AuNPs-siRNA-OCH₃ 50 nM (figure 17, panel B), respectively. A significant decrease in FITC intensity was noted for AuNPs-PEG.siRNA when compared to AuNPs-FA.siRNA. In addition, particles were only observed in sections ranging from $-2\ \mu\text{m}$ to $+1\ \mu\text{m}$ in cells incubated with AuNPs-FA.siRNA, while they were completely absent in cells incubated with AuNPs-PEG.siRNA. Furthermore, a 2D render series of 1 frame/second was created to demonstrate this phenomenon (video S1, data not shown). These findings clearly indicate that our AuNPs are in fact penetrating the cell surface and residing in the cytoplasm.

V. Discussion

Since AuNPs possess sensitive SPR resonance, minute changes to the NP colloidal solutions during synthesis was easily picked up via DLS-ZETA measurements and UV-vis spectroscopy. In addition, manipulating the concentration of AuNPs-d-PLL synthesis components, such as HAuCl₄, d-PLL, and Asc Ac, yielded expected results. Firstly, it was evident that as the concentration of gold precursor increased (from 0.125 mM to 1 mM), the Z avg of our AuNPs-d-PLL also increased (from 50.45 ± 0.28 nm to 125.0 ± 2.6 nm). This is expected assuming we have the same number of nuclei initially formed, thus allowing the particles to grow larger in size. This phenomenon has been previously reported by Maruyama T. et al (2015) while demonstrating an increase in Gold-Histidine particles with increasing AuCl₄⁻ concentration [196]. With regards to the effect of d-PLL concentration on particle size, as the concentration of d-PLL increased, the size of the particles increased, as well (from 66.84 ± 0.94 nm at 1 μ M d-PLL, to 82.71 ± 2.51 nm at 12 μ M d-PLL). This behavior was not expected since more polymer will be available, with increased concentration, to be adsorbed on the surface of the particles, thus controlling their size and aggregation, and preventing the growth of gold nuclei. Finally, concerning the effect of our reducing agent on the size of AuNPs-d-PLL, the reverse effect was observed. Particles synthesized using excess 1 Asc Ac proved the largest (Z avg) measuring at 89.92 ± 2.05 nm, while particles synthesized with excess 5 Asc Ac had the smallest hydrodynamic diameter (64.65 ± 0.42 nm). This occurs because, depending on the strength of the reducing agent used, more gold nuclei will form resulting in smaller NPs. This process has also been documented by Maruyama T. et al (2015), as their Gold-Histidine NPs behaved quite similarly with their size decreasing as the concentration of Histidine (reducing agent) increased [196].

Folate receptors are cellular membrane glycoproteins, comprising of three isoforms: namely FR α , FR β and FR γ [18]. Folate receptors bind folic acid and structurally similar folic acid derivatives and mediate cellular delivery of these compounds. It has been established that folate receptors are overexpressed on many malignant tissues including PC, while their expression is minimal in

healthy tissues [17, 18]. Targeted delivery via folate receptors can be utilized to increase the efficacy and reduce the toxicity of medicinal agents for cancer therapy [19]. In this study, folic acid (FA) was chosen as a targeting ligand, and the ability to attach FA to the AuNPs as a delivery vector for siRNA was investigated.

Furthermore, the safety and biocompatibility of our carriers was demonstrated using a WST-1 assay. Contrary to common belief, our positively charged AuNPs did not possess any cytotoxic effects at 50 μ g/mL on PC3 cells, even after 24 hours of incubation. As it has been previously reported that positively charged cetyltrimethyl ammonium bromide (CTAB) capped AuNPs are cytotoxic even at their lowest concentration (0.05 μ M) [197, 198]. Furthermore, PEGylation of our nanocomplex certainly contributed to its low cytotoxicity profile, as neutral polymers are known to enhance NP biocompatibility [199].

The strong positively charged nature of our AuNPs allowed for easier complexation with the negatively charged FAM siRNA, via ionic charge interaction. Indeed, DLS findings summarized in table 2, further validate this notion. The noticeable increase in size (Z avg) of AuNPs-d-PLL-PEG-FA (from 125.5 \pm 5nm to 136 \pm 1.5 nm), and the dramatic decrease in ZETA potential from (+) 30 \pm 0.9 mV to (-) 11.5 \pm 1.5 mV, post siRNA addition (50 nM) strongly indicate the successful complexation of siRNA to our functionalized targeted carriers. Additionally, agarose gel retardation allowed us to visualize this complexation *in-situ*. As in the case of AuNPs-d-PLL, the particles were shown to possess a high positive charge of (+) 32 \pm 1.3 mV. This allowed them to complex siRNA even at a low MR. As evident by gel electrophoresis; complexation is apparent at MR 10, but completely achieved at MR 30. For AuNPs-d-PLL that have been slightly neutralized with PEG-OCH₃, these particles had the least positive zeta potential, which resulted in a fainter band at MR 10 when compared to AuNPs-d-PLL. However, as the MR of AuNPs-d-PLL-OCH₃ to siRNA increased, complexation increased as well, until it was fully achieved at MR 30. Finally, with regards to siRNA complexation with AuNPs-d-PLL-

FA, these particles presented a ZETA potential which is slightly less positive than AuNPs-d-PLL. The complexation pattern of these particles should be similar to that of AuNPs-d-PLL. However, since FA as a molecule is larger, it is suggested that it causes some steric interference, hindering the complexation with siRNA, resulting in slightly more visible bands when compared to panels A and B at MR 10 [17]. Nonetheless, complete AuNPs-d-PLL-FA.siRNA complexation was achieved at MR 30. These results corroborate previous findings by J. Guo et al, 2016, where their PEI-capped AuNPs behaved similarly, achieving complete siRNA complexation only at MR 20 and onwards for AuNPs-PEI-FA [17]. This data so far, indicates that our NP complexes can easily and successfully complex siRNA for potential *in-vitro* cargo delivery irrespective of the coating agent used during their synthesis.

Flow cytometry was a follow up to the electrophoresis to detect the optimum siRNA concentration for internalization and to provide evidence that FA samples bind to PC3-PSMA cells unlike the OCH3 samples. When comparing side scattering among the samples, no significant difference was noted. This might be due to the negative surface charge of our NPs, post siRNA complexation, causing slight repulsion with the negatively charged lipid bilayer of the cells [200]. However, a clear increase in FL-1 intensity was present, especially for cells incubated with AuNPs-d-PLL-FA.siRNA at 50 nM. This suggests that our AuNPs were able to bypass said repulsion as their ZETA potential post siRNA complexation was nearly neutral (table 2) When incubated with AuNPs-d-PLL-PEG.siRNA at either 25 or 50 nM siRNA concentration, minimal fluorescence was detected ($\leq 5\%$). This indicates that AuNPs-d-PLL-OCH3.siRNA do not bind to PSMA or folate receptors localized on the surface of PC3 cells. On the other hand, cells incubated with AuNPs-d-PLL-FA.siRNA (25 nM) presented a mean percent fluorescence of $\sim 17\%$, indicating some interaction with PC3-PSMA cells. Finally, cells incubated with AuNPs-d-PLL-FA.siRNA (50 nM) had the highest mean percent fluorescence, indicating that our AuNPs-FA complexes exhibit a specific binding capacity to

FA receptors located on the cell surface of PC3-PSMA cells [201] and that a 50 nM concentration of siRNA is adequate for intracellular localization.

Laser scanning microscopy was challenging since it was difficult to pinpoint the exact method of AuNP uptake. PC3-PSMA cells were incubated with AuNPs-FA.siRNA at 50 nM and AuNPs-OCH3.siRNA at 50 nM. Cells with AuNPs-FA showed vesicle-like formations while cells incubated with AuNPs.OCH3 showed almost no siRNA signal. This is an indication of particle internalization. However, it was not enough to surely claim that the particles reside inside the cytoplasm. Thus, cells were then incubated again with AuNPs.FA.siRNA and AuNPs-OCH3.siRNA at 50nM, respectively. However, we stained the cells with EEA-1 1/100 and M6PR 1/150 to visualize the particles enclosed within either early endosomes or lysosomes. After many trials, we were unable to observe an overlapping signal for either EEA-1 or M6PR with siRNA. At first glance, we thought that the particles were not internalized. However, vesicle-like formations in cells incubated with AuNPs.FA.siRNA were observed. Figure 16, D and E, overlay demonstrated that a low percentage of cells exhibited yellow overlap zones post AuNPs-FA.siRNA incubation. Furthermore, our Z-stacks clearly demonstrated that cells incubated with AuNPs-FA.siRNA possessed highly fluorescent structures, while cells transfected with AuNPs-OCH3.siRNA did not. This implied that something was occurring upon AuNP internalization that allowed the escape of siRNA into the cell's cytoplasm.

Upon further investigation, we speculated that when nanoparticles coated with positively charged, low pka amino groups, such as PEI or d-PLL enter cells, they experience a process called the sponge effect [202]. Upon bypassing the cell's lipid bilayer, these cationic NPs enter acidic vesicles, where their amino groups sequester protons supplied by the proton pump, v-ATPase. Furthermore, the sequestered protons cause the pump to remain functioning, leading to the retention of chloride ions and water molecules. Finally, osmotic swelling causes rupture of the vesicles, allowing the cationic NPs to enter the cell's cytoplasm [203]. This phenomenon has

been noted repeatedly with NPs possessing a positively charged coating and is generally an acceptable hypothesis when dealing with positively charged polymers like PEI and its derivatives [204]. This process is also observed with d-PLL coated AuNPs since they behaved similarly. Additionally, our data was also supportive of Guo, J., et al., 2016 findings, as their PEI-capped NPs showed endosomal escape and free-floating siRNA was observed in the cytoplasm after a four-hour incubation period [17].

VI. Conclusion and Future Perspectives

Manipulating the AuNPs-d-PLL synthesis reaction components yielded expected results. The increase in HAuCl_4 concentrations resulted in an increase in Z_{avg} , while an increase in L -ascorbic acid concentration, yielded smaller particles. However, data collected from increasing d-PLL concentration effect on AuNPs size was inconclusive. Furthermore, our AuNPs exhibited selective and specific binding while preserving stable delivery of siRNA. Thus, our vehicles provide another dimension beyond siRNA delivery. They are suitable to be conjugated to therapeutic agents as delivery vectors and enhance their uptake by the targeted malignant tissues. Furthermore, PEGylating our particles certainly improved their cytotoxicity and tolerance by live PC3-PSMA cells *in-vitro*. However, further studies are still needed to examine the output of our knock-out siRNA delivery. This could be by targeting specific genes present in PC3 cells and determining, using RT-PCR, their expression levels post-treatment with our AuNPs. Furthermore, implementing live cellular imaging and intracellular trafficking techniques might shed some light on the exact internalization pathway employed by our AuNPs.

Tables

Table 1. Characterization of AuNPs-d-PLL synthesized under three different conditions via Dynamic Light Scattering, ZETA measurements and UV-Vis Spectrophotometry. All samples were diluted to the lowest sample concentration prior to analysis. Readings were performed in triplicates in disposable folded capillary tubes (DLS-ZETA) and black quartz cuvettes (UV-Vis) (n = 3).

Effect of Increasing [HAuCl₄] on AuNP size

[HAuCl ₄]	PDI	Z avg (d.nm)	Size I (d.nm)	Size N (d.nm)	Zeta Potential (mV)	A max (a.m.u)	λ max (nm)
0.125 mM	0.232 ± 0.014	50.45 ± 0.28	63.69 ± 0.52	33.33 ± 5.55	(+) 23.3 ± 4.1	0.5468	543
0.25 mM	0.198 ± 0.032	69.49 ± 0.77	86.77 ± 3.64	37.16 ± 8.7	(+) 25 ± 0.6	0.5431	551
0.5 mM	0.148 ± 0.008	90.82 ± 2.81	106.3 ± 3.2	54.64 ± 4.9	(+) 31.4 ± 1.4	0.5624	571
1 mM	0.097 ± 0.04	125.0 ± 2.6	137.6 ± 4.2	99.09 ± 7.25	(+) 40.8 ± 1.2	0.2847	602

Effect of Increasing [d-PLL] on AuNP size

[d-PLL]	PDI	Z avg (d.nm)	Size I (d.nm)	Size N (d.nm)	Zeta Potential (mV)	A max (a.m.u)	λ max (nm)
1 μM	0.184 ± 0.021	66.84 ± 0.94	82.29 ± 1.11	36.60 ± 5.28	(+) 37.5 ± 0.9	1.1413	570
3 μM	0.180 ± 0.024	70.19 ± 1.99	83.38 ± 1.63	44.58 ± 6.42	(+) 35.5 ± 1.1	1.1426	571
6 μM	0.184 ± 0.026	70.88 ± 0.72	87.54 ± 3.97	43.51 ± 10.89	(+) 32.9 ± 1.1	1.1644	580
12 μM	0.164 ± 0.026	82.71 ± 2.51	99.43 ± 1.97	51.11 ± 9.38	(+) 36.6 ± 2.5	1.0221	597

Effect of increasing [Asc Ac] on AuNP size

[Asc Ac]	PDI	Z avg (d.nm)	Size I (d.nm)	Size N (d.nm)	Zeta Potential (mV)	A max (a.m.u)	λ max (nm)
ex 1	0.160 ± 0.032	89.92 ± 2.05	104.7 ± 2.5	57.27 ± 8.75	(+) 36.5 ± 1.2	1.0757	595
ex 1.55	0.171 ± 0.029	80.31 ± 2.41	94.12 ± 3.12	51.56 ± 4.55	(+) 32.5 ± 1.8	1.1139	573
ex 3	0.178 ± 0.059	74.03 ± 1.32	88.80 ± 5.48	50.23 ± 19.81	(+) 30.5 ± 3.2	1.0799	566
ex 5	0.186 ± 0.023	64.65 ± 0.42	78.04 ± 2.8	46.94 ± 13.8	(+) 28.5 ± 0.33	1.1174	554

Table 2. Characterization of AuNPs-d-PLL, PEG, and FA for siRNA Delivery via Dynamic Light Scattering, ZETA measurements and UV-Vis Spectrophotometry. Readings were performed in triplicates in disposable folded capillary tubes (n = 3).

NPs	PdI	Z avg (d.nm)	Size I (d.nm)	Size N (d.nm)	Zeta Potential (mV)	A max (a.m.u)	λ max (nm)
AuNPs-d-PLL	0.097 ± 0.005	118.8 ± 1	131 ± 1	89 ± 1	(+) 32 ± 1.3	0.5183	572
AuNPS-d-PLL- PEG	0.083 ± 0.02	133.1 ± 0.9	144.4 ± 0.3	114.13 ± 8	(+) 21 ± 1	0.5647	578
AuNPs-d-PLL-FA	0.091 ± 0.033	125.5 ± 5	143.3 ± 3	113.9 ± 10	(+) 30 ± 0.9	0.5156	576

NPs	PdI	Z avg (d.nm)	Size I (d.nm)	Size N (d.nm)	Zeta Potential (mV)
AuNPs-d- PLL.siRNA 25 nM	0.160 ± 0.043	123.5 ± 2.2	132.43 ± 7	94.26 ± 2	(-) 21.13 ± 0.5
AuNPs-d-PLL- PEG.siRNA 25 nM	0.094 ± 0.010	135 ± 4	149 ± 3	111.6 ± 12.5	(-) 14.13 ± 4.87
AuNPs-d-PLL- FA.siRNA 25 nM	0.113 ± 0.022	193.5 ± 1.9	213.43 ± 7.53	187.33 ± 1.67	(-) 11.41 ± 3.78

NPs	PdI	Z avg (d.nm)	Size I (d.nm)	Size N (d.nm)	Zeta Potential (mV)
AuNPs-d- PLL.siRNA 50 nM	0.207 ± 0.023	139.6 ± 1.3	168.7 ± 14.3	81.94 ± 7.94	(-) 23.6 ± 2
AuNPs-d-PLL- PEG.siRNA 50 nM	0.146 ± 0.015	134 ± 1	147.9 ± 6.1	94.47 ± 10	(-) 4.4 ± 1.4
AuNPs-d-PLL- FA.siRNA 50 nM	0.207 ± 0.020	136 ± 1.5	166.3 ± 14.3	78.6 ± 7.78	(-) 11.5 ± 1.5

Figures

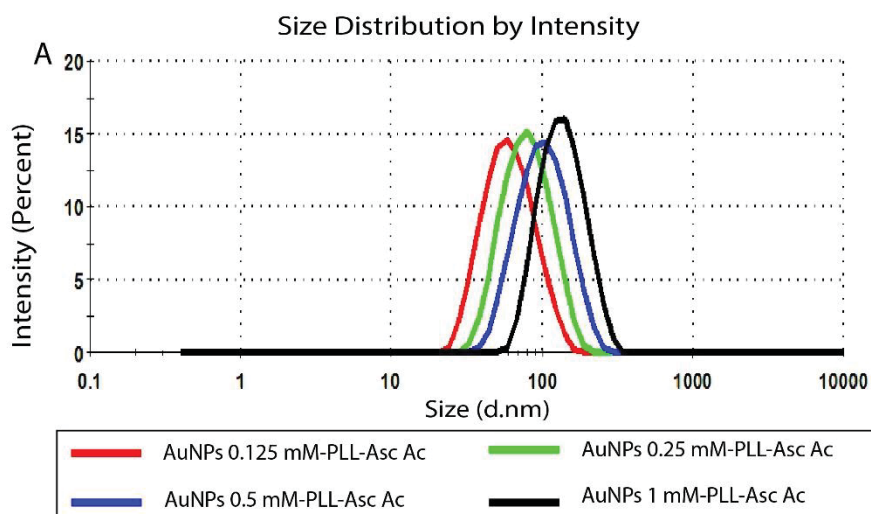


Figure 1. Effect of increasing [HAuCl₄] on Size Distribution by Intensity of AuNPs-d-PLL. An increase in size, of 19 nm, was observed when comparing AuNPs at 0.125 mM HAuCl₄ in red (50.45 ± 0.28) to AuNPs at 0.25 mM HAuCl₄ in green (69.49 ± 0.77). Similarly, AuNPs at 0.5 mM HAuCl₄, represented in blue, had an increase in size of 21 nm when compared to AuNPs at 0.25 mM (90.82 ± 2.81 vs. 69.49 ± 0.77). Finally, particles synthesized at 1 mM HAuCl₄ (in black) presented an increase of 35 nm and had the largest size of all the previously mentioned particles (125.0 ± 2.6) ($n = 3$).

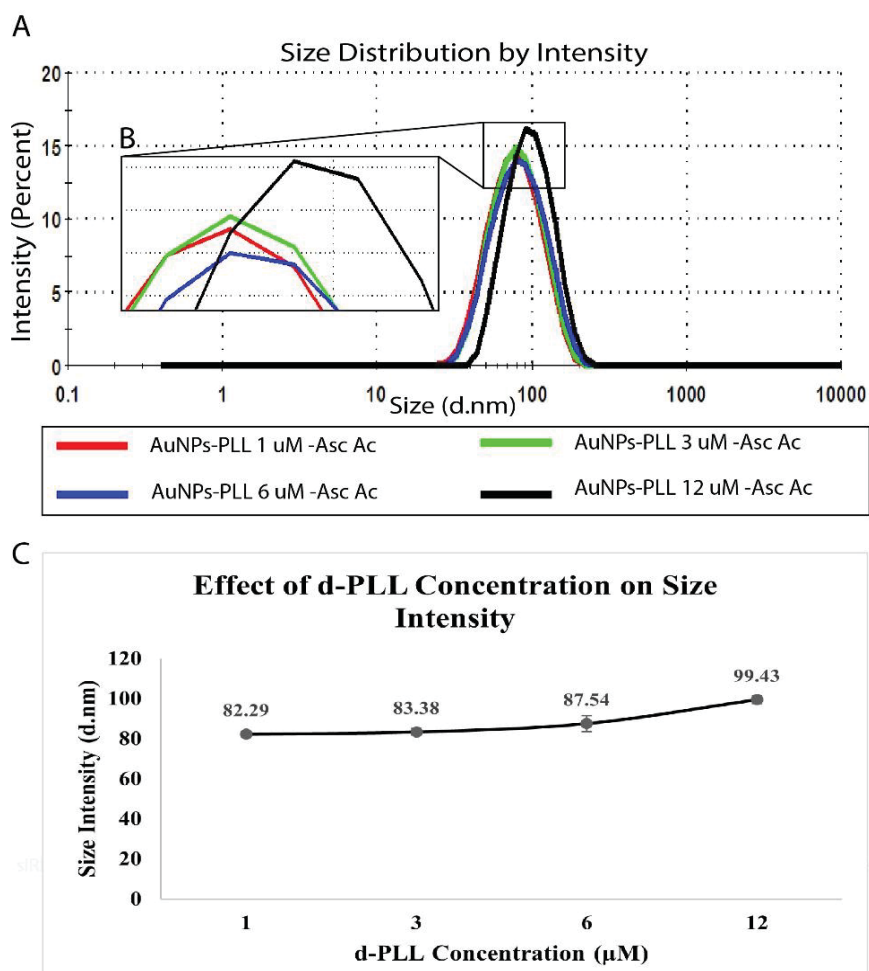


Figure 2. Effect of increasing [d-PLL] on Size Distribution by Intensity of AuNPs-d-PLL. Panel A: A small increase of 4 nm in Z avg was noted when comparing NPs synthesized using 1 µM d-PLL (red line) to particles synthesized using 3 µM d-PLL (green line) (66.84 ± 0.94 vs. 70.19 ± 1.99 respectively). A non-significant increase in size of about 1 nm was observed when increasing d-PLL concentration to 6 µM (blue line). Finally, the largest increase in Z avg (12 nm) was observed for particles synthesized using 12 µM d-PLL (black line). Panel B: Inset of enlarged peaks to clarify the variation in size. Panel C: Line chart showing the effect of [d-PLL] on size intensity distribution of AuNPs-d-PLL. A clear increase in Size I (1 nm, 4 nm, and 12 nm respectively) is observed with increasing d-PLL concentration.

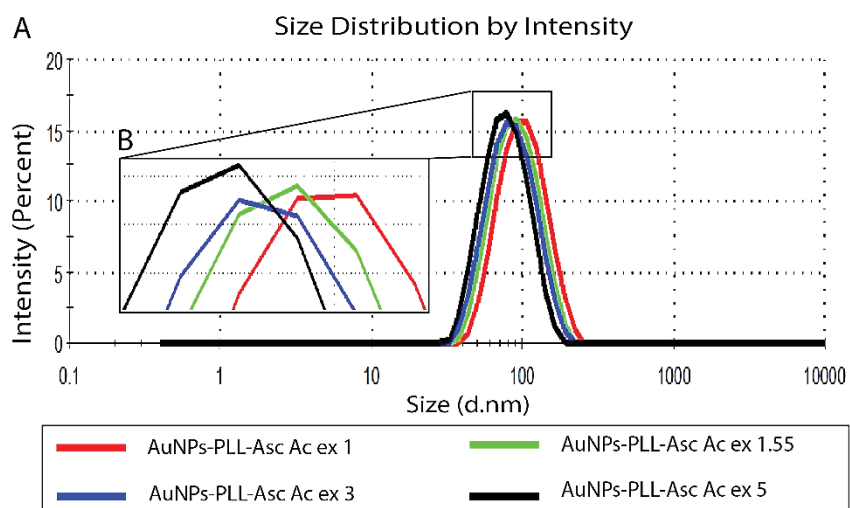


Figure 3. Effect of increasing [Asc Ac] on Size Distribution by Intensity of AuNPs-d-PLL. Panel A: A decrease of 9 nm was observed when comparing AuNPs at excess 1 Asc Ac in red (89.92 ± 2.05), to AuNPs at excess 1.55 Asc Ac in green (80.31 ± 2.41). When increasing Asc Ac to excess 3 (blue line), the particles further decreased in size reaching 74.03 ± 1.32 nm vs. 80.31 ± 2.41 nm. Finally, with excess 5 Asc Ac in black, the largest decrease in size (10 nm) was noted, and the particles reached the smallest size of 64.65 ± 0.42 as compared to the rest of the batch. Panel B: Inset of enlarged peaks to clarify the change in size.

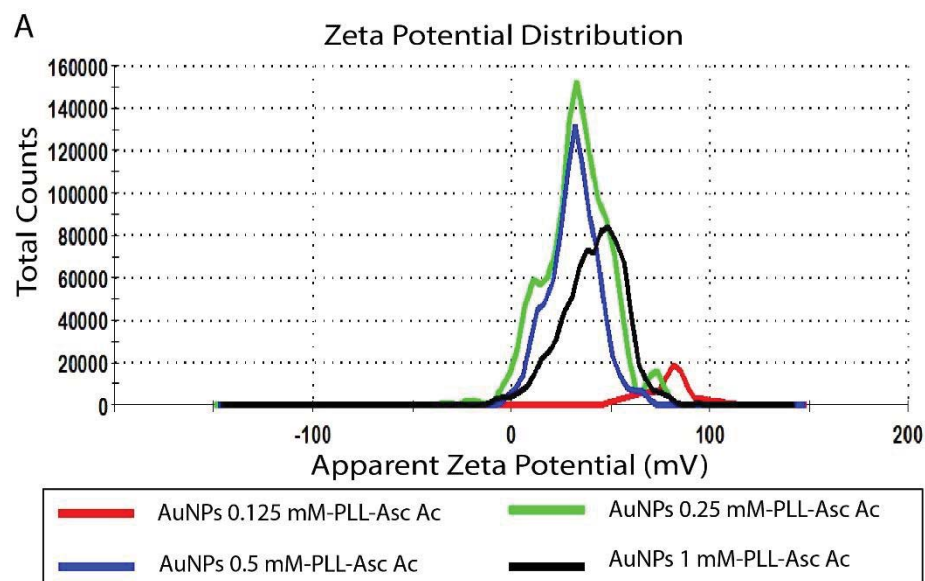


Figure 4. Effect of increasing [HAuCl₄] on Zeta Potential of AuNPs-d-PLL. AuNPs synthesized with 0.125 mM HAuCl₄ (red curve) had the lowest zeta potential of (+) 23.3 ± 4.1 mV. As the concentration of HAuCl₄ increased, the zeta potential of the particles increased as well, reaching (+) 25 ± 0.6 mV for particles synthesized at 0.25 mM (green curve), (+) 31.4 ± 1.4 mV for particles at 0.5 mM HAuCl₄ (green curve), and finally (+) 40.8 ± 1.2 mV for particles synthesized at 1 mM HAuCl₄ in black.

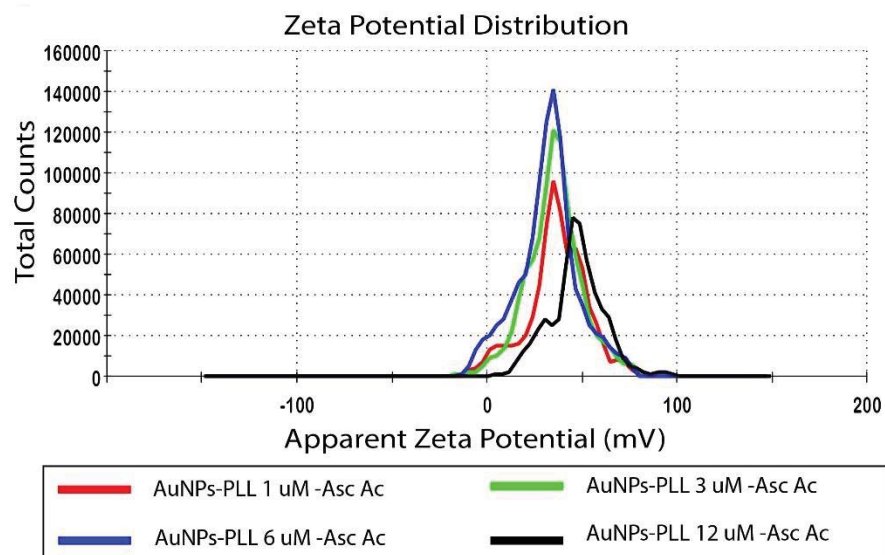


Figure 5. Effect of increasing [d-PLL] on Zeta Potential of AuNPs-d-PLL. No significant variation in the apparent zeta potential of AuNPs-d-PLL was noted. However, all synthesized particles possessed a zeta potential larger than (+) 30 mV, with the average zeta potential recorded at (+) 34 ± 3 mV.

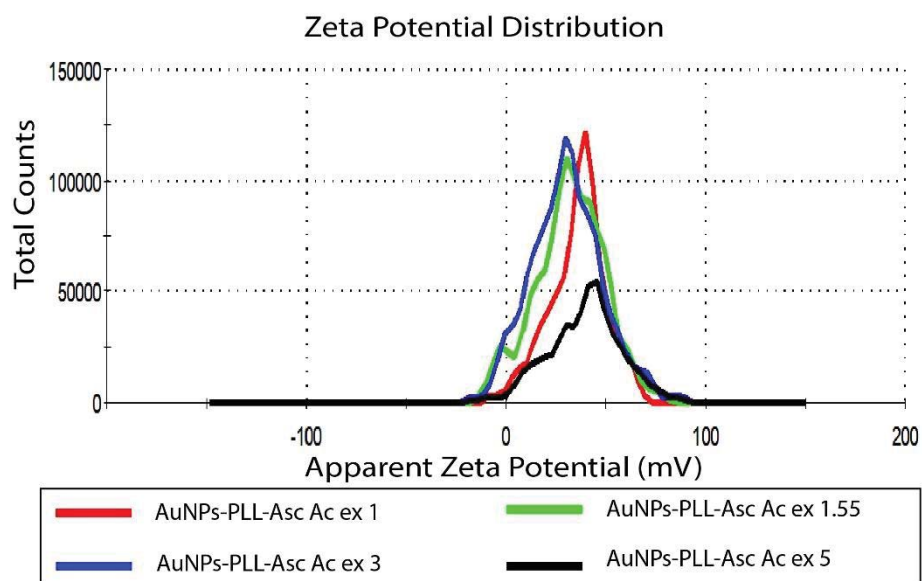


Figure 6. Effect of increasing [Asc Ac] on Zeta Potential of AuNPs-d-PLL. No significant effect of Asc Ac concentration on the apparent zeta potential of AuNPs-d-PLL was noted. However, all synthesized particles possessed a zeta potential larger than (+) 20 mV, with the average zeta potential recorded at (+) 32 ± 4 mV.

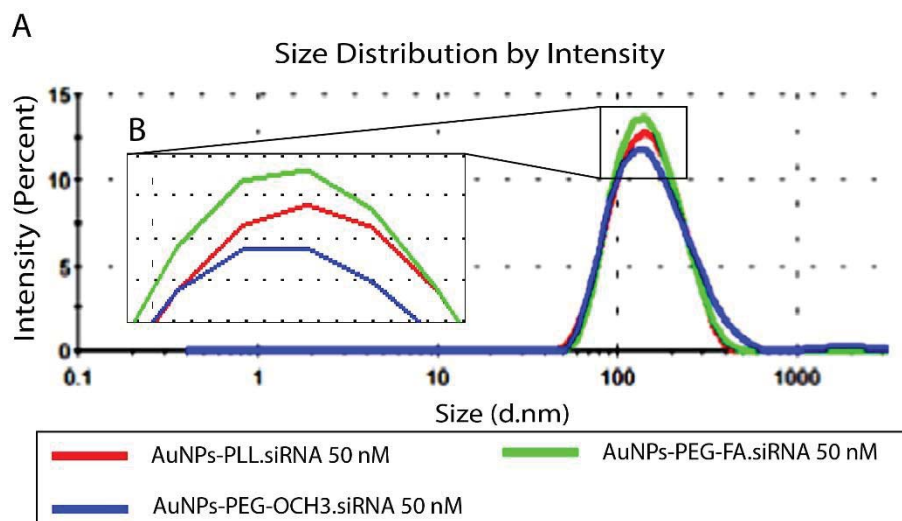


Figure 7. Size distribution by Intensity of AuNPs-d-PLL Vs. AuNPs-d-PLL-PEG-OCH3 and AuNPs-d-PLL-PEG-FA. Panel A: An increase of 7 nm in size by intensity was noted when comparing AuNPs-d-PLL in red curve (118.8 ± 1) to AuNPs-d-PLL-PEG-FA in green curve (125.5 ± 5). An increase of 15 nm in size by intensity was observed when comparing AuNPs-d-PLL (118.8 ± 1) to AuNPs-d-PLL-PEG-OCH3 in blue curve (133.1 ± 0.9). Panel B: Inset of enlarged peaks to clarify the variation in size ($n = 3$).

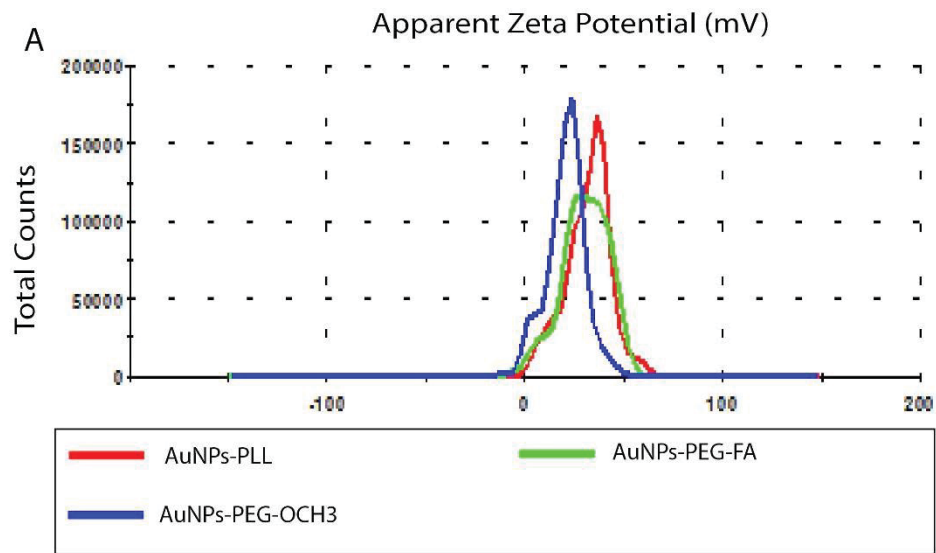


Figure 8. Zeta measurements of AuNPs-d-PLL Vs. AuNPs-d-PLL-PEG-OCH3 and AuNPs-d-PLL-PEG-FA. AuNPs-d-PLL-PEG-OCH3 recorded the lowest charge at 21 ± 1 mV when compared to AuNPs-d-PLL 32 ± 1.3 mV, and AuNPs-d-PLL-PEG-FA (30.2 ± 0.9). A 2 mV decrease in zeta potential was observed between AuNPs-d-PLL and AuNPs-d-PLL-PEG-FA ($n = 3$).

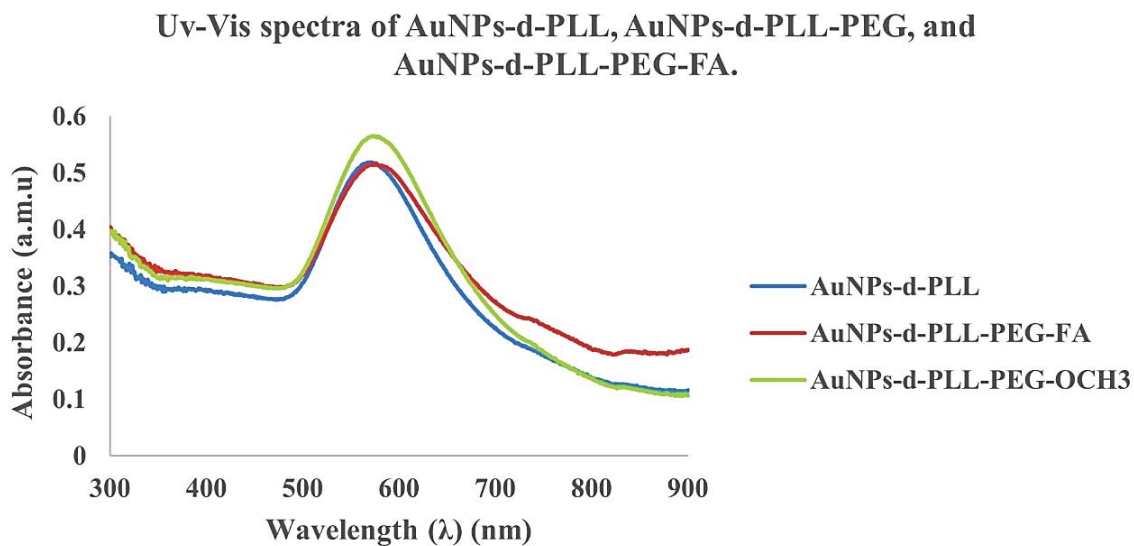


Figure 9. Uv-Vis spectra of AuNPs-d-PLL, AuNPs-d-PLL-PEG, and AuNPs-d-PLL-PEG-FA.

A clear red shift of 4 nm (AuNPs-d-PLL-FA), and of 6 nm (AuNPs-d-PLL-PEG) is noted upon the addition of PEG-FA and PEG-OCH₃ to AuNPs-d-PLL. (n = 3)

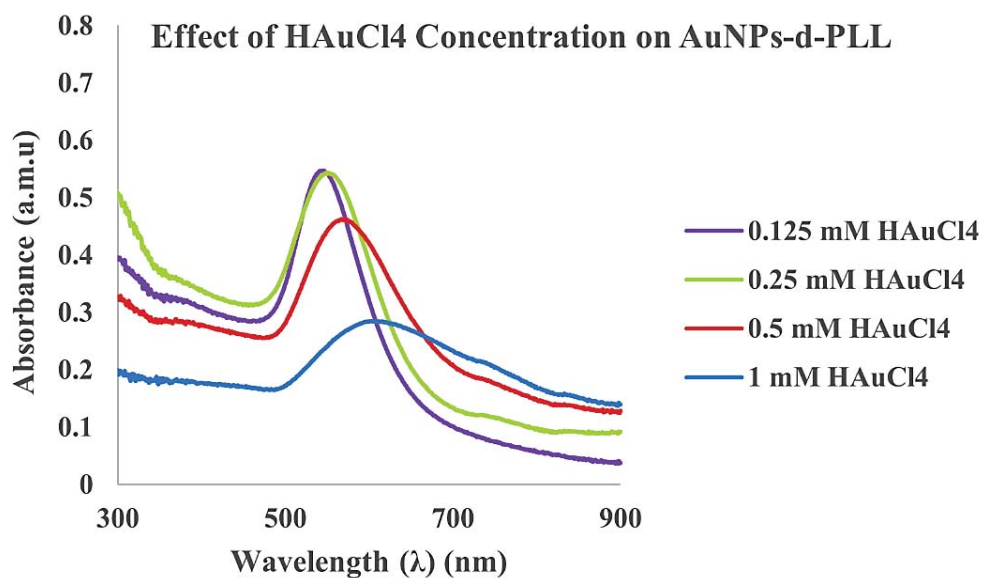


Figure 10. Uv-Vis Spectra of AuNPs-d-PLL Synthesized with Increasing H_{AuCl}₄ Concentrations. A clear shift to the right of 8 nm was observed when comparing AuNPs at 0.125 mM H_{AuCl}₄ (purple line) to AuNPs at 0.25 mM (green line). Similarly, a red shift of 20 nm is observed when increasing [H_{AuCl}₄] to 0.5 mM (red line). Finally, the shift in wavelength was most noticeable with 1 mM H_{AuCl}₄ (blue line) (31 nm). All samples were diluted to the lowest sample concentration (n = 3).

Effect of d-PLL Concentration on AuNPs-d-PLL

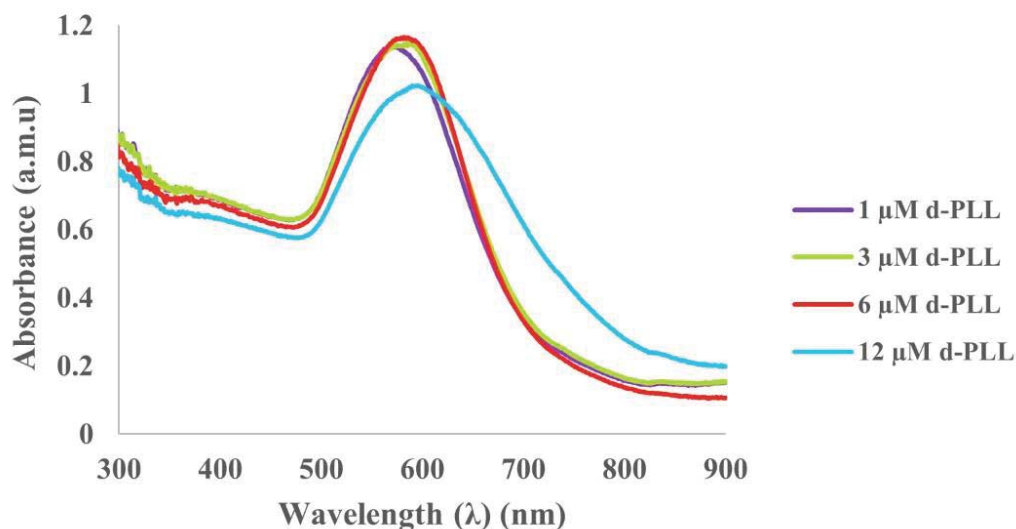


Figure 11. Uv-Vis Spectra of AuNPs-d-PLL Synthesized with Increasing d-PLL Concentrations.

A small red shift of only 1 nm was recorded for AuNPs synthesized at 3 μM d- PLL (green line) when compared to AuNPs at 1 μM d- PLL (purple line). This shift further increased to the right (9 nm) with AuNPs at 6 μM (red line). Finally, the largest shift in wavelength was recorded for AuNPs-d-PLL synthesized at 12 μM d-PLL (blue line) (17 nm). All samples have been diluted to the lowest sample concentration (n = 3).

Effect of Increasing Asc Ac Concentration on AuNPs-d-PLL

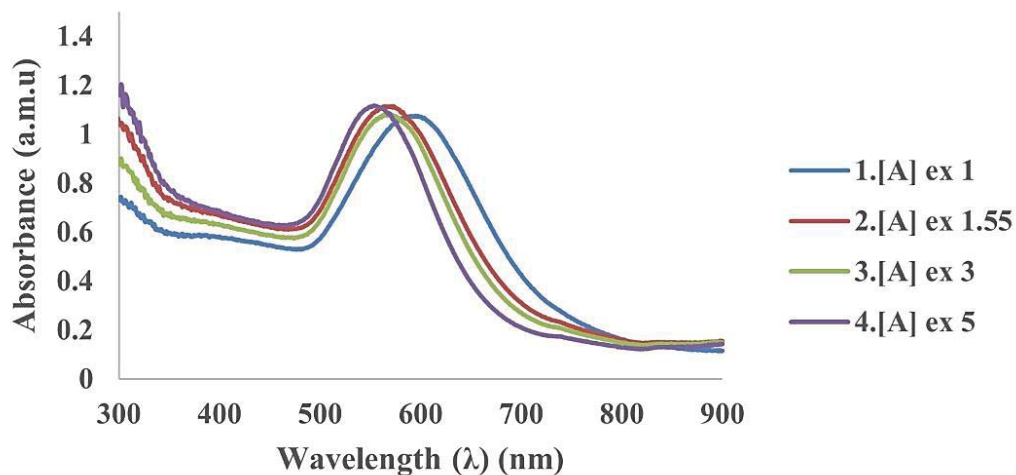


Figure 12. UV-Vis Spectra of AuNPs-d-PLL Synthesized with Increasing Asc Ac Concentrations. A large blue shift of 22 nm was noticed when comparing AuNPs-d-PLL at excess 1 Asc Ac (blue line) to AuNPs-d-PLL synthesized with ex 1.55 Asc Ac (red line). This shift further increased to the left (7 nm) for AuNPs-d-PLL Asc Ac ex 3 (green line). The largest blue shift (41 nm) was noted for AuNPs-d-PLL synthesized at ex 5 Asc Ac (purple line) relative to AuNPs-d-PLL at ex 1 Asc Ac. All samples have been diluted to the lowest sample concentration ($n = 3$).

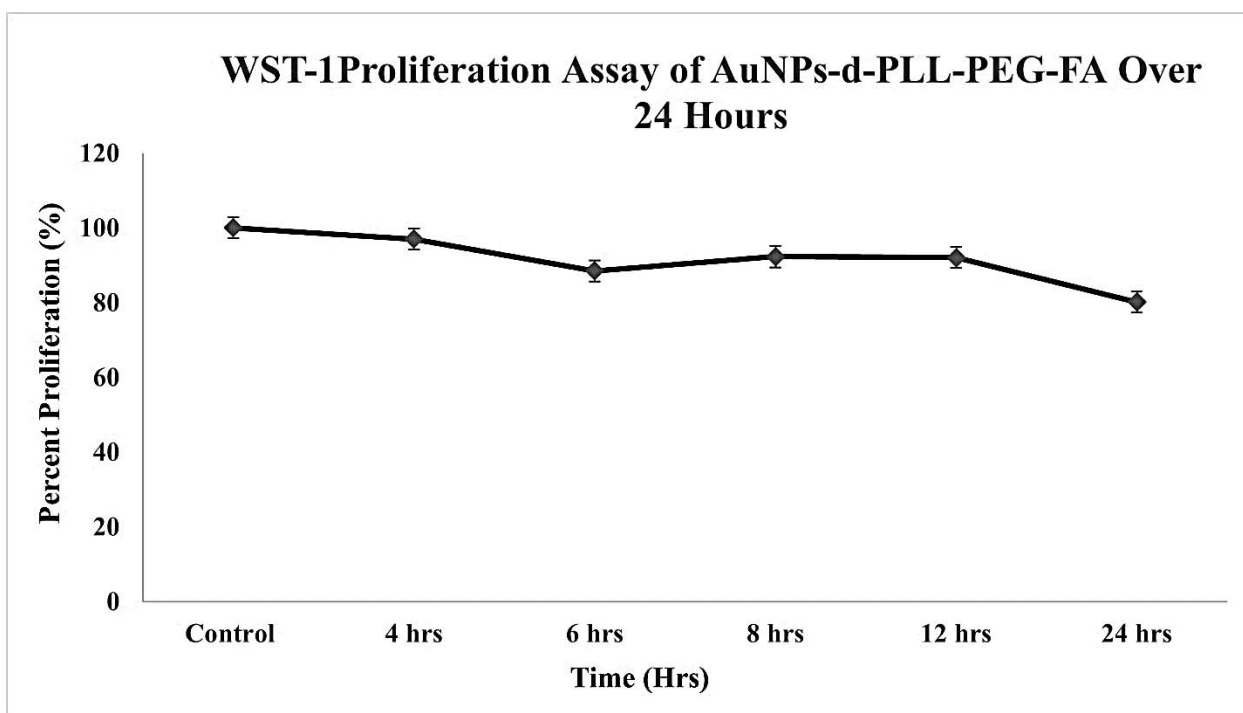


Figure 13. WST-1 Cell Proliferation Assay of AuNPs-d-PLL-PEG-FA. The line chart demonstrates the cytotoxicity profile of AuNPs-d-PLL-PEG-FA when incubated with PC3-PSMA cells over a period of 24 hours. NP concentration was fixed at 50 $\mu\text{g}/\text{mL}$ for all time points. Cells were initially seeded onto a 96-well plated and were left to reach confluency prior to the assay, then incubated with 50 $\mu\text{g}/\text{mL}$ AuNPs-d-PLL-PEG-FA for four, six, eight, 12, and 24 hours. Absorbance was read at 450 nm.

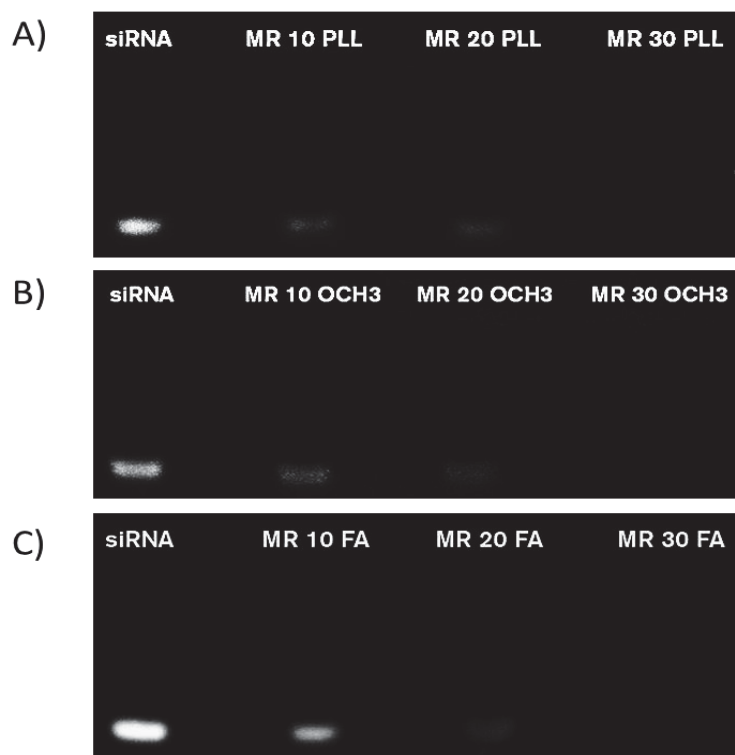


Figure 14. Agarose gel electrophoresis of various AuNPs.siRNA MRs captured under UV light with ChemiDoc™. siRNA (0.25 $\mu\text{g/mL}$) was used as a control (first lane in all panels). AuNPs.siRNA complexation was observed on a 1.5% agarose gel with various coating: AuNPs-d-PLL (A), AuNP-d-PLL-PEG-OCH₃ (B), and AuNPs-d-PLL-PEG-FA (C) at MRs (10, 20 and 30). A clear decrease in band intensity was visible at MR 20. At MR 30, the siRNA band entirely disappeared in all three samples indicating a successful and complete complexation. (n = 5)

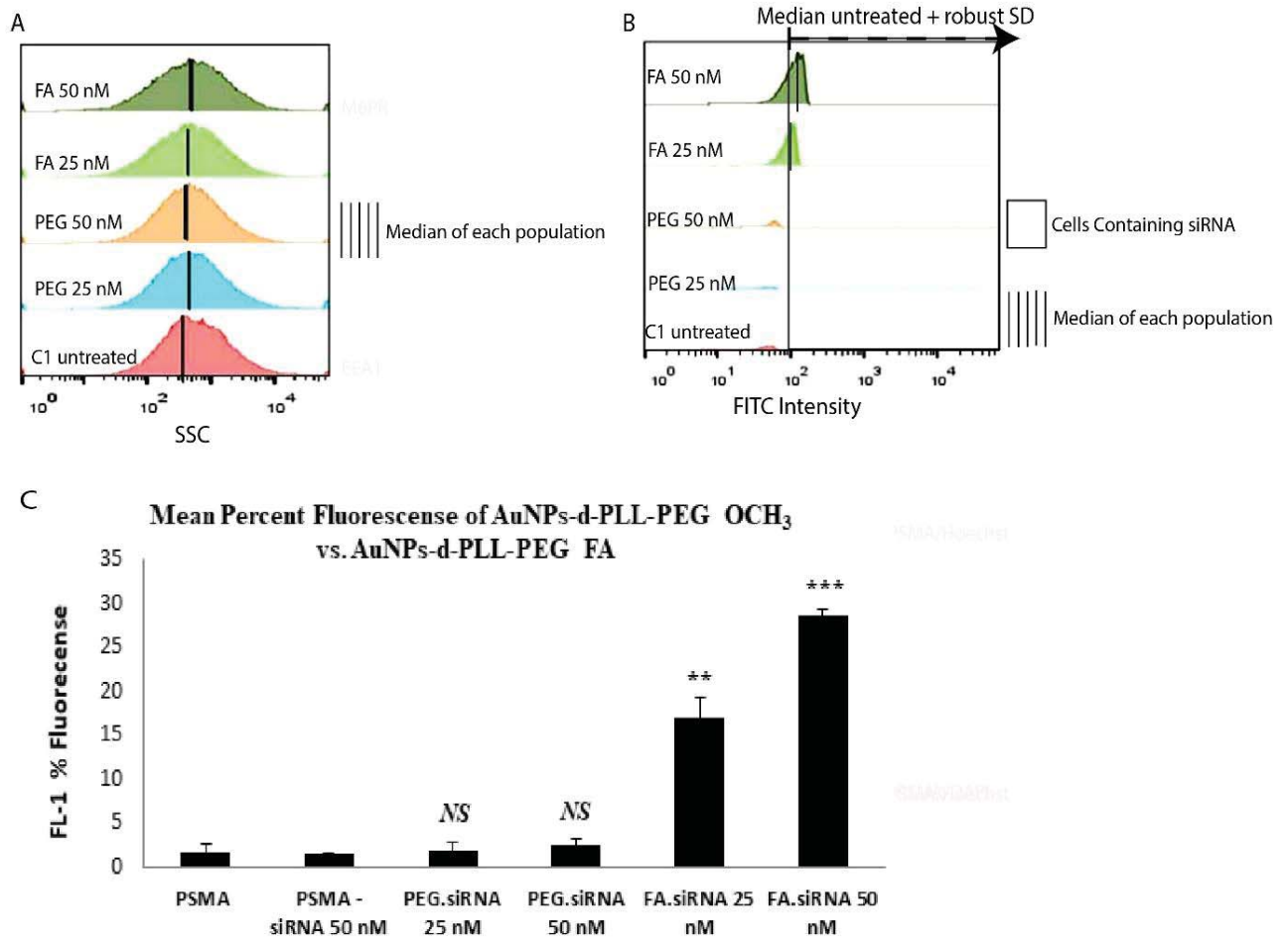


Figure 15. Mean Percent Fluorescence of AuNPs-d-PLL-PEG OCH₃ vs. AuNPs-d-PLL-PEG-FA. PC3-PSMA cells and PC3-PSMA.siRNA (50nM) were used as control. Cells incubated with siRNA.AuNPs-d-PLL-PEG (25 and 50nM) showed insignificant fluorescence ($\leq 5\%$). Cells incubated with siRNA.AuNPs-d-PLL-FA (25 nM) presented a mean percent fluorescence of $\sim 17\%$, while increasing siRNA.AuNPs-d-PLL-FA to 50 nM had the highest mean percent fluorescence of $\sim 30\%$ ($n = 3$).

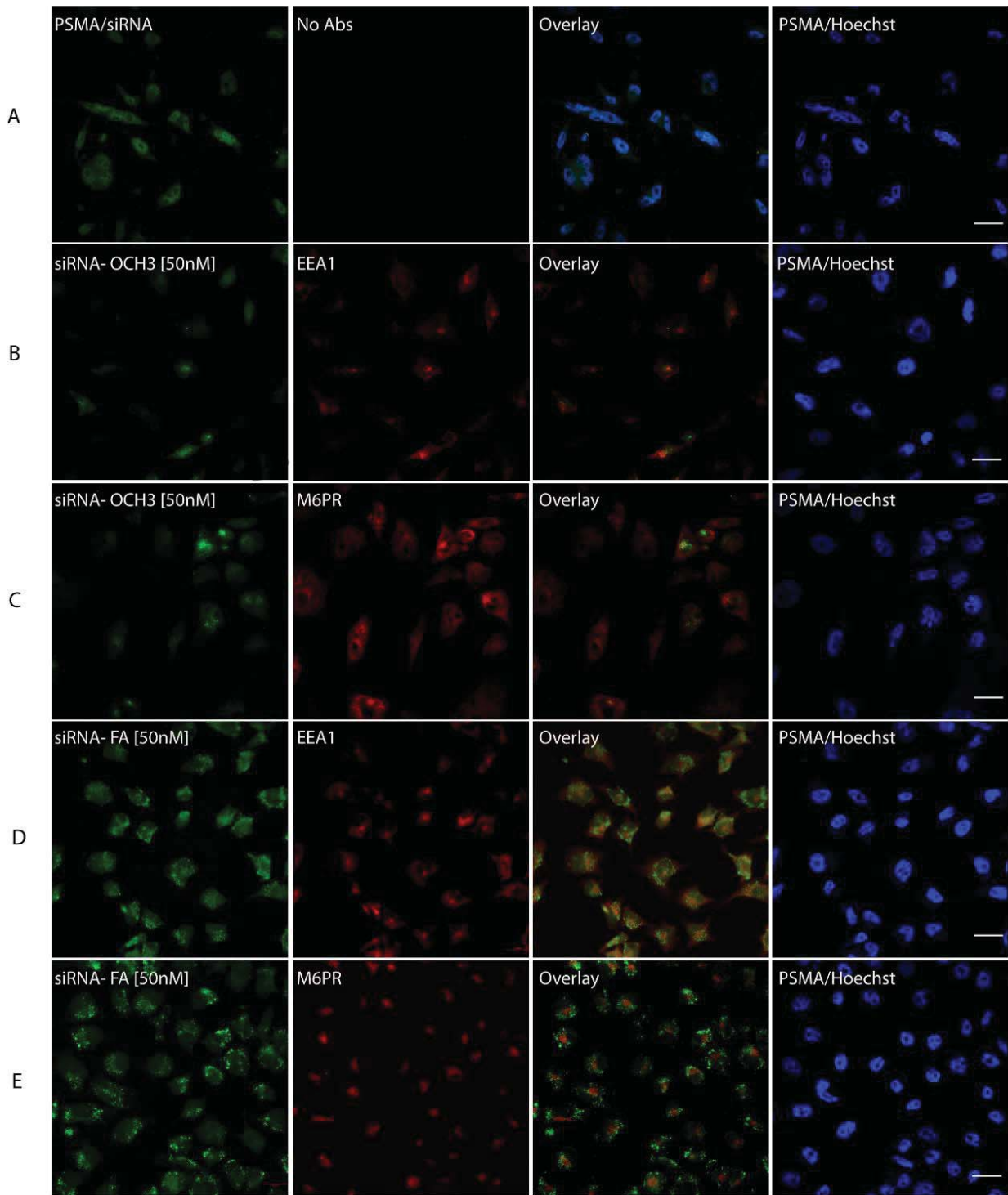


Figure 16. siRNA intracellular localization. PC3-PSMA cells were incubated for 4 hours with siRNA.NP complexes tagged with either -OCH3 (B, C) or -FA (D, E) at 37 °C. Panel A serves as a control, where PC3-PSMA cells were incubated with 50nM siRNA only. Cells were fixed in 100%

methanol at -20 °C for 5 min and then stained with Hoechst along with anti-early endosomal (EEA1 1/100) or lysosomal (M6PR 1/150) markers. Pattern of siRNA co-localization was visualized by Zeiss Confocal microscopy mainly from the overlay images. Only overlay from panel D showed dot-like structures with partial resemblance to early endosomes in almost 30% of the tested cells with siRNA-NP-FA-50 (D). Scale bar set at 20 μm (n=5 /panel).

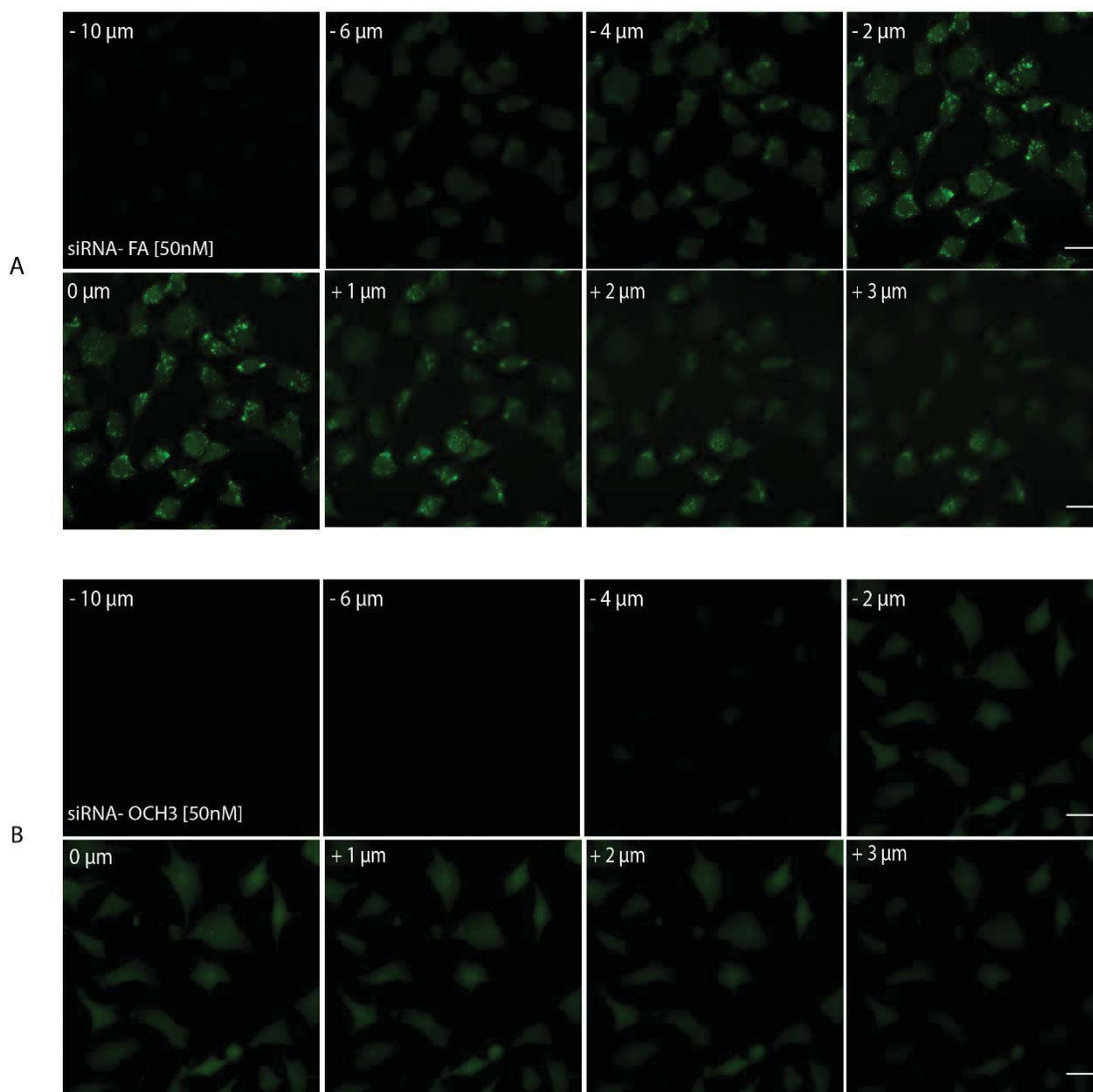


Figure 17. Z-stack imaging of PSMA cells treated with AuNPs-PEG.siRNA (50 nM) Vs. AuNPs-FA.siRNA (50 nM). Eight out of 20 sections were chosen as representatives. Sections ranged from $-10 \mu\text{m}$ to $+10 \mu\text{m}$. All lasers had the same pin hole. Gain was set at 650 nm for FITC and 550 nm for Hoechst. A noticeable decrease in FITC intensity of AuNPs-PEG.siRNA when compared to AuNPs-FA.siRNA was noted. Furthermore, particles were only visible in sections ranging from $-2 \mu\text{m}$ to $+1 \mu\text{m}$ in cells incubated with (A); particles were absent in cells incubated with AuNPs-PEG.siRNA. Scale bar was set at $20 \mu\text{m}$ ($n = 3$).

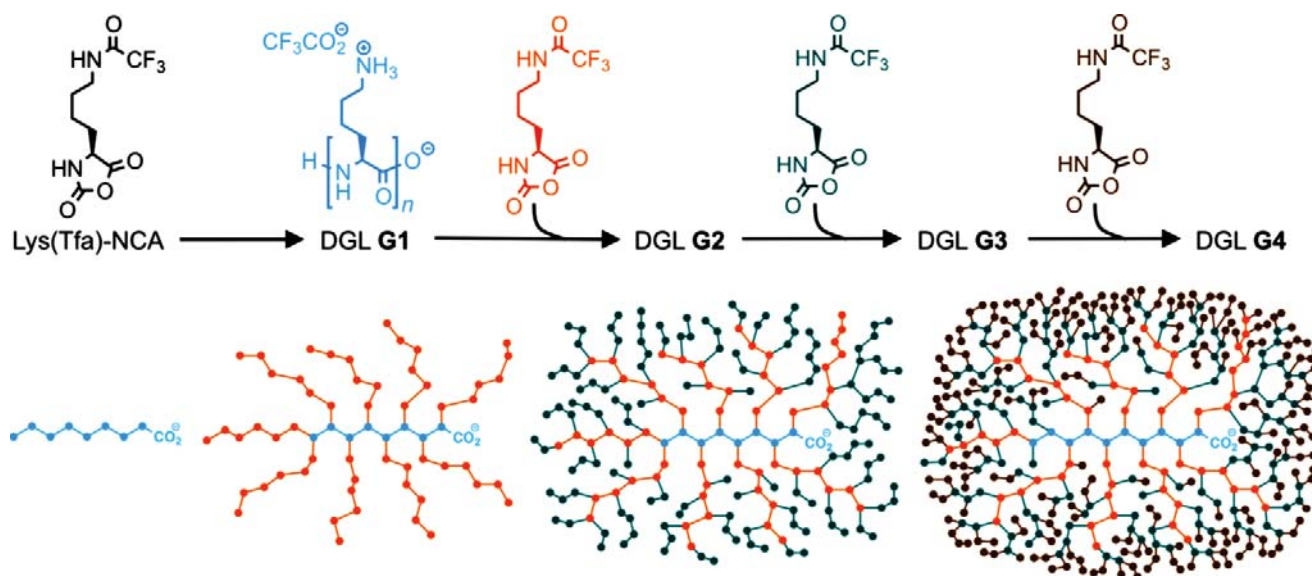


Figure 18. The synthetic route to first- to fourth-generation DGLs G1-G4, as well as their schematic representation (each dot represents a L-lysine residue, pending free amino groups are not represented). Each generation's synthesis involves the following steps: Polycondensation in water, centrifugation to collect the precipitate, alkaline deprotection of the side chains, and concentration (retrieved from: <https://hal.archives-ouvertes.fr/hal-01814843> by Francoia Jean-Patrick, 2018)

VII. References

1. Siegel, R.L., et al., *Cancer Statistics, 2021*. CA Cancer J Clin, 2021. **71**(1): p. 7-33.
2. K. Rahme, J.G., S. Biswas, C. M. O'Driscoll, and J. D. Holmes, *Branched PEI Capped Gold Nanoparticles in Water for siRNA Delivery to Cancer Cells*. Advanced Materials: TechConnect Briefs 2017: p. 159-162.
3. Rahme, K., et al., *PEGylated gold nanoparticles: polymer quantification as a function of PEG lengths and nanoparticle dimensions*. RSC Adv., 2013. **3**(17): p. 6085-6094.
4. Sajid, M.I., et al., *Overcoming Barriers for siRNA Therapeutics: From Bench to Bedside*. Pharmaceuticals (Basel), 2020. **13**(10).
5. Guo, J., et al., *Positively charged, surfactant-free gold nanoparticles for nucleic acid delivery*. RSC Advances, 2015. **5**(23): p. 17862-17871.
6. Hu, B., et al., *Therapeutic siRNA: state of the art*. Signal Transduct Target Ther, 2020. **5**(1): p. 101.
7. Bai, D.P., et al., *Zinc oxide nanoparticles induce apoptosis and autophagy in human ovarian cancer cells*. Int J Nanomedicine, 2017. **12**: p. 6521-6535.
8. Cabrera, M.P., et al., *Highly fluorescent and superparamagnetic nanosystem for biomedical applications*. Nanotechnology, 2017. **28**(28): p. 285704.
9. Condello, M., et al., *ZnO nanoparticle tracking from uptake to genotoxic damage in human colon carcinoma cells*. Toxicol In Vitro, 2016. **35**: p. 169-79.
10. Pathakoti, K., M. Manubolu, and H.M. Hwang, *Nanostructures: Current uses and future applications in food science*. J Food Drug Anal, 2017. **25**(2): p. 245-253.
11. Mainini, F. and M.R. Eccles, *Lipid and Polymer-Based Nanoparticle siRNA Delivery Systems for Cancer Therapy*. Molecules, 2020. **25**(11).
12. Hanley, C., et al., *The Influences of Cell Type and ZnO Nanoparticle Size on Immune Cell Cytotoxicity and Cytokine Induction*. Nanoscale Res Lett, 2009. **4**(12): p. 1409-20.
13. Rattan, R., et al., *Nanoparticle-macrophage interactions: A balance between clearance and cell-specific targeting*. Bioorg Med Chem, 2017. **25**(16): p. 4487-4496.
14. Boisselier, E. and D. Astruc, *Gold nanoparticles in nanomedicine: preparations, imaging, diagnostics, therapies and toxicity*. Chem Soc Rev, 2009. **38**(6): p. 1759-82.
15. Karin A Binnemars-Postma, H.W.t.H., Gert Storm, and Jai Prakash, *Differential uptake of nanoparticles by human M1 and M2 polarized macrophages: protein corona as a critical determinant*. Nanomedicine, 2016.
16. Connor, E.E., et al., *Gold nanoparticles are taken up by human cells but do not cause acute cytotoxicity*. Small, 2005. **1**(3): p. 325-7.
17. Guo, J., et al., *Bioconjugated gold nanoparticles enhance cellular uptake: A proof of concept study for siRNA delivery in prostate cancer cells*. Int J Pharm, 2016. **509**(1-2): p. 16-27.
18. Xiaobin Zhao , H.L.R.J.L., *Targeted drug delivery via folate receptors*. Expert Opin. Drug Deliv., 2008: p. 309-319.
19. Scomparin, A., et al., *A comparative study of folate receptor-targeted doxorubicin delivery systems: dosing regimens and therapeutic index*. J Control Release, 2015. **208**: p. 106-20.
20. Collet, H., et al., *An expeditious multigram-scale synthesis of lysine dendrigraft (DGL) polymers by aqueous N-carboxyanhydride polycondensation*. Chemistry, 2010. **16**(7): p. 2309-16.
21. Toivanen, R. and M.M. Shen, *Prostate organogenesis: tissue induction, hormonal regulation and cell type specification*. Development, 2017. **144**(8): p. 1382-1398.
22. V. L. KUMAR, P.K.M., *Prostate Gland: Structure, Functions and Regulation*. International Urology and Nephrology, 1995. **27**(3): p. 231-243.
23. Garraway, I.P., et al., *Human prostate sphere-forming cells represent a subset of basal epithelial cells capable of glandular regeneration in vivo*. The Prostate, 2010. **70**(5): p. 491-501.

24. Chen, S.L., et al., *Prostate Cancer Mortality-To-Incidence Ratios Are Associated with Cancer Care Disparities in 35 Countries*. Sci Rep, 2017. **7**: p. 40003.
25. Jemal, A., et al., *Global patterns of cancer incidence and mortality rates and trends*. Cancer Epidemiol Biomarkers Prev, 2010. **19**(8): p. 1893-907.
26. A.Loeb, K.R.L.a.L., *Significance of multiple mutations in cancer*. Carcinogenesis, 2000. **21**(3): p. 379-385.
27. Roberts, M.J., et al., *Prostate Cancer Detection*, in *Endotext*, K.R. Feingold, et al., Editors. 2000, MDText.com, Inc.Copyright © 2000-2021, MDText.com, Inc.: South Dartmouth (MA).
28. Bubendorf, L., et al., *Metastatic patterns of prostate cancer: an autopsy study of 1,589 patients*. Hum Pathol, 2000. **31**(5): p. 578-83.
29. Gann, P.H., *Risk Factors for Prostate Cancer*. Reviews in Urology, 2002. **4**: p. S3-S10.
30. Yin Sun, J.N., and Jiaoti Huang, *Neuroendocrine differentiation in prostate cancer*. Am J Transl Res, 2009. **1**(2): p. 148-162.
31. Vashchenko, N. and P.A. Abrahamsson, *Neuroendocrine differentiation in prostate cancer: implications for new treatment modalities*. Eur Urol, 2005. **47**(2): p. 147-55.
32. Bonkhoff, H., *Neuroendocrine differentiation in human prostate cancer. Morphogenesis, proliferation and androgen receptor status*. Ann Oncol, 2001. **12 Suppl 2**: p. S141-4.
33. Huang, J., et al., *Immunohistochemical characterization of neuroendocrine cells in prostate cancer*. Prostate, 2006. **66**(13): p. 1399-406.
34. Alukal, J.P. and H. Lepor, *Testosterone Deficiency and the Prostate*. Urol Clin North Am, 2016. **43**(2): p. 203-8.
35. Pan, M.H., et al., *Biodistributions of 177Lu- and 111In-labeled 7E11 antibodies to prostate-specific membrane antigen in xenograft model of prostate cancer and potential use of 111In-7E11 as a pre-therapeutic agent for 177Lu-7E11 radioimmunotherapy*. Mol Imaging Biol, 2009. **11**(3): p. 159-66.
36. van Rij, C.M., et al., *Pretargeted Radioimmunotherapy of Prostate Cancer with an Anti-TROP-2xAnti-HSG Bispecific Antibody and a (177)Lu-Labeled Peptide*. Cancer Biother Radiopharm, 2014. **29**(8): p. 323-9.
37. Elgqvist, J., *Nanoparticles as Theranostic Vehicles in Experimental and Clinical Applications-Focus on Prostate and Breast Cancer*. Int J Mol Sci, 2017. **18**(5).
38. Daniyal, M., et al., *Epidemiology, etiology, diagnosis and treatment of prostate cancer*. Asian Pac J Cancer Prev, 2014. **15**(22): p. 9575-8.
39. Bostwick, D.G., et al., *Human prostate cancer risk factors*. Cancer, 2004. **101**(10 Suppl): p. 2371-490.
40. Mottet, N., et al., *Implementing newer agents for the management of castrate-resistant prostate cancer: what is known and what is needed?* BJU Int, 2015. **115**(3): p. 364-72.
41. Wolf, A.M., et al., *American Cancer Society guideline for the early detection of prostate cancer: update 2010*. CA Cancer J Clin, 2010. **60**(2): p. 70-98.
42. SKOLNICK, D.T.B.A.M.H., *Genetic Epidemiology of Cancer in Utah Genealogies: A Prelude to the Molecular Genetics of Common Cancers*. JOURNAL OF CELLULAR PHYSIOLOGY, 1984: p. 63-77.
43. BOB S. CARTER, T.H.B., GARY D. STEINBERG, BARTON CHILDS, AND PATRICK C. WALSH, *Mendelian inheritance of familial prostate cancer* Proc. Natl. Acad. Sci., 1992. **89**: p. 3367-3371.
44. Henrik Gronberg, L.D., and Jan Erik Damber, *Familial Prostate Cancer in Sweden A Nationwide Register Cohort Study*. American Cancer Society, 1996: p. 138-143.
45. Camp, N.J., J.M. Farnham, and L.A. Cannon-Albright, *Localization of a prostate cancer predisposition gene to an 880-kb region on chromosome 22q12.3 in Utah high-risk pedigrees*. Cancer Res, 2006. **66**(20): p. 10205-12.
46. Ledet, E.M., et al., *Suggestive evidence of linkage identified at chromosomes 12q24 and 2p16 in African American prostate cancer families from Louisiana*. Prostate, 2012. **72**(9): p. 938-47.
47. Kolonel, L.N., D. Altshuler, and B.E. Henderson, *The multiethnic cohort study: exploring genes, lifestyle and cancer risk*. Nat Rev Cancer, 2004. **4**(7): p. 519-27.

48. GuocanWang, D.Z., Denise J. Spring, and Ronald A. DePinho, *Genetics and biology of prostate cancer*. Genes & Development, 2018. **32**: p. 1105-1140.
49. Parnham, A. and E.C. Serefoglu, *Retrograde ejaculation, painful ejaculation and hematospermia*. Transl Androl Urol, 2016. **5**(4): p. 592-601.
50. Nieder, C., et al., *Pathologic fracture and metastatic spinal cord compression in patients with prostate cancer and bone metastases*. BMC Urol, 2010. **10**: p. 23.
51. Suzman, D.L., S.A. Boikos, and M.A. Carducci, *Bone-targeting agents in prostate cancer*. Cancer Metastasis Rev, 2014. **33**(2-3): p. 619-28.
52. CRAWFORD, E.D., *EPIDEMIOLOGY OF PROSTATE CANCER*. UROLOGY, 2003. **62**.
53. Barbara Frigerio, G.F., Elena Luison, Alessandro Satta, Ettore Seregn, Marco Colombatti, Giulio Fracasso, Riccardo Valdagni, Delia Mezzanzanica, Otto Boerman, Silvana Canevari, and Mariangela Figini, *Full preclinical validation of the 123 I-labeled anti-PSMA antibody fragment ScFvD2B for prostate cancer imaging*. Oncotarget, 2017. **8**(7): p. 10919-10930.
54. CATALONA, D.S.S.a.W.J., *INTEREXAMINER VARIABILITY OF DIGITAL RECTAL EXAMINATION IN DETECTING PROSTATE CANCER*. UROLOGY, 1995. **45**(1).
55. Machulkin, A.E., et al., *Nanohybride Materials Based on Magnetite-Gold Nanoparticles for Diagnostics of Prostate Cancer: Synthesis and In Vitro Testing*. Bull Exp Biol Med, 2016. **161**(5): p. 706-710.
56. Ayyildiz, S.N. and A. Ayyildiz, *PSA, PSA derivatives, proPSA and prostate health index in the diagnosis of prostate cancer*. Turk J Urol, 2014. **40**(2): p. 82-8.
57. Ian M. Thompson, D.K.P., Phyllis J. Goodman, Catherine M. Tangen, M. Scott Lucia, Howard L. Parnes, Lori M. Minasian, Leslie G. Ford, Scott M. Lippman, E. David Crawford, John J. Crowley, and Charles A. Coltman, Jr., *Prevalence of Prostate Cancer among Men with a Prostate-Specific Antigen Level ≤ 4.0 ng per Milliliter*. The New England Journal of Medicine, 2004. **350**(22): p. 2239-2246.
58. Eton, D.T. and S.J. Lepore, *Prostate cancer and health-related quality of life: a review of the literature*. Psychooncology, 2002. **11**(4): p. 307-26.
59. Klaus Braun , V.E., Manfred Wiessler, Ruediger Pipkorn, Bernd Didinger, Gabriele Mueller, and Waldemar Waldeck and *High-Resolution Flow Cytometry: a Suitable Tool for Monitoring Aneuploid Prostate Cancer Cells after TMZ and TMZ-BioShuttle Treatment*. International Journal of Medical Sciences, 2009. **6**(6): p. 338-347.
60. Peyromaure, M., et al., *[Characteristics of prostate cancer in men less than 50-year-old]*. Prog Urol, 2009. **19**(11): p. 803-9.
61. Ibrahim, T., et al., *Pathogenesis of osteoblastic bone metastases from prostate cancer*. Cancer, 2010. **116**(6): p. 1406-18.
62. N. Lawrentschuk, G.T., C. Kuk and A.R. Zlotta, *Role of surgery in high-risk localized prostate cancer* Current Oncology, 2010. **17**: p. S25-S32.
63. Donnelly, B.J., et al., *A randomized trial of external beam radiotherapy versus cryoablation in patients with localized prostate cancer*. Cancer, 2010. **116**(2): p. 323-30.
64. A.J. Hayden, C.C., and T. Pickles, *Radiation therapy in prostate cancer: a risk-adapted strategy*. Current Oncology, 2010. **17**(2): p. 18-24.
65. Lepor, M.A.P.a.H., *Androgen Deprivation Therapy in the Treatment of Advanced Prostate Cancer*. Reviews in Urology, 2007. **9**(1): p. 53-58.
66. Sun, H., et al., *Oligonucleotide aptamers: new tools for targeted cancer therapy*. Mol Ther Nucleic Acids, 2014. **3**: p. e182.
67. Sanna, V. and M. Sechi, *Nanoparticle therapeutics for prostate cancer treatment*. Nanomedicine, 2012. **8 Suppl 1**: p. S31-6.
68. Forbes, L.J., et al., *Risk factors for delay in symptomatic presentation: a survey of cancer patients*. Br J Cancer, 2014. **111**(3): p. 581-8.

69. Anil K. Patri, A.M., James Beals, Thommey P. Thomas, Neil H. Bander, and and J. James R. Baker, *Synthesis and in Vitro Testing of J591 Antibody-Dendrimer Conjugates for Targeted Prostate Cancer Therapy*. Bioconjugate Chem, 2004. **15**: p. 1174-1181.
70. Kaittanis, C., et al., *Targetable Clinical Nanoparticles for Precision Cancer Therapy Based on Disease-Specific Molecular Inflection Points*. Nano Lett, 2017. **17**(11): p. 7160-7168.
71. Chakraborty, S. and T. Rahman, *The difficulties in cancer treatment*. Ecancermedalscience, 2012. **6**: p. ed16.
72. Langut, Y., et al., *PSMA-targeted polyinosine/polycytosine vector induces prostate tumor regression and invokes an antitumor immune response in mice*. Proc Natl Acad Sci U S A, 2017. **114**(52): p. 13655-13660.
73. Ron S. Israeli, C.T.P., John G. Corr, William R. Fair, and Warren D. W. Heston, *Expression of the Prostate-specific Membrane Antigen* Cancer Research, 1994. **54**: p. 1807-1811.
74. SAM S. CHANG, V.E.R., W. D. W. HESTON, AND PAUL B. GAUDIN, *COMPARISON OF ANTI-PROSTATE-SPECIFIC MEMBRANE NTIGEN ANTIBODIES AND OTHER IMMUNOMARKERS IN ETASTATIC PROSTATE CARCINOMA*. UROLOGY, 2001. **57**(6): p. 1179-1183.
75. Horoszewicz, J., *MONOCLONAL ANTIBODIES TO NEW ANTIGENIC MARKER IN PITHELIAL PROSTATIC CELLS AND SERUM OF PROSTATIC CANCER CELLS*. PATIENT ABSTRACTS, 1993.
76. J Leek, N.L., B Maraj, A Bailey, IM Carr, S Andersen, J Cross, P Whelan, KA MacLennan, DM Meredith and AF Markham, *Prostate-specific membrane antigen: evidence for the existence of a second related human gene*. Br J Cancer, 1995. **72**: p. 583-588.
77. Juliana Denekamp, A.D., and Anthony Waites, *VACULATURE AND MICROENVIRONMENTAL GRADIENTS: THE MISSING LINKS IN NOVEL APPROACHES TO CANCER THERAPY?* Advan Enzyme Regul, 1998. **38**: p. 281-299.
78. Rajasekaran, A.K., G. Anilkumar, and J.J. Christiansen, *Is prostate-specific membrane antigen a multifunctional protein?* Am J Physiol Cell Physiol, 2005. **288**(5): p. C975-81.
79. Denise S. O'Keefe , S.L.S., Dean J. Bacich, Yutaka Horiguchi, Ying Luo,, et al., *Mapping, genomic organization and promoter analysis of the human prostate-speciçc membrane antigen gene*. Biochimica et Biophysica Acta, 1998. **1443**: p. 113-127.
80. Virgolini, I., et al., *Current status of theranostics in prostate cancer*. Eur J Nucl Med Mol Imaging, 2018. **45**(3): p. 471-495.
81. Backhaus, P., et al., *Targeting PSMA by radioligands in non-prostate disease-current status and future perspectives*. Eur J Nucl Med Mol Imaging, 2018. **45**(5): p. 860-877.
82. David A. Silver, I.P., William R. Fair, Warren D. W. Heston, and Carlos Cordon-Cardo, *Prostate-specific Membrane Antigen Expression in Normal and Malignant Human Tissues*. Clinical Cancer Research, 1997. **3**: p. 81-87.
83. Ristau, B.T., D.S. O'Keefe, and D.J. Bacich, *The prostate-specific membrane antigen: lessons and current clinical implications from 20 years of research*. Urol Oncol, 2014. **32**(3): p. 272-9.
84. Kaighn, M.E., et al., *Establishment and characterization of a human prostatic carcinoma cell line (PC-3)*. Invest Urol, 1979. **17**(1): p. 16-23.
85. Keer, H.N., et al., *Elevated Transferrin Receptor Content in Human Prostate Cancer Cell Lines Assessed in Vitro and in Vivo*. Journal of Urology, 1990. **143**(2): p. 381-385.
86. ZETTER, M.C.R.A.B.R., *Selective stimulation of prostatic carcinoma cell proliferation by transferrin*. Proc. Natl. Acad. Sci., 1992. **89**: p. 6197-6201.
87. Hiroyuki Yamazaki, E.S., Charles E. Myers, and Birandra K. Sinha, *Oncogene overexpression and de novo drug-resistance in human prostate cancer cells*. Biochimica et Biophysica Acta, 1994. **1226**: p. 89-96.
88. Huang, I.P., et al., *Enhanced chemotherapy of cancer using pH-sensitive mesoporous silica nanoparticles to antagonize P-glycoprotein-mediated drug resistance*. Mol Cancer Ther, 2011. **10**(5): p. 761-9.
89. van Bokhoven, A., et al., *Molecular characterization of human prostate carcinoma cell lines*. Prostate, 2003. **57**(3): p. 205-25.

90. Barlaam, B., et al., *Discovery of (R)-8-(1-(3,5-difluorophenylamino)ethyl)-N,N-dimethyl-2-morpholino-4-oxo-4H-chromene-6-carboxamide (AZD8186): a potent and selective inhibitor of PI3Kbeta and PI3Kdelta for the treatment of PTEN-deficient cancers*. J Med Chem, 2015. **58**(2): p. 943-62.
91. Hironori Tashiro, M.S.B., Rong Wu, Kathleen R. Cho, Shikha Bose, Steven I. Wang, Jing Li, and a.L.H.E. Ramon Parsons, *Mutations in PTEN Are Frequent in Endometrial Carcinoma But Rare in Other Common Gynecological Malignancies*. Cancer Research, 1997. **57**: p. 3933-3940.
92. Paul Cairns, E.E., Kenji Okami, Naomi Halachmi, Manel Esteller, James G Herman, and S.I.W. Shikha Bose, Ramon Parsons and David Sidransky, *Point mutation and homozygous deletion of PTEN/MMAC1 in primary bladder cancers*. Oncogene, 1998. **16**: p. 3215-3218.
93. Steven I. Wang, R.P., and Michael Ittmann, *Homozygous Deletion of the PTEN Tumor Sppressor Gene in a Sbset of Postate Aenocarcinomas*. Clinical Cancer Research, 1998. **4**: p. 811-815.
94. Buzea, C., Pacheco, II, and K. Robbie, *Nanomaterials and nanoparticles: sources and toxicity*. Biointerphases, 2007. **2**(4): p. MR17-71.
95. Ahmed, N., H. Fessi, and A. Elaissari, *Theranostic applications of nanoparticles in cancer*. Drug Discov Today, 2012. **17**(17-18): p. 928-34.
96. Rizzo, L.Y., et al., *Recent progress in nanomedicine: therapeutic, diagnostic and theranostic applications*. Curr Opin Biotechnol, 2013. **24**(6): p. 1159-66.
97. Abolfazl Akbarzadeh, R.R.-S., Soodabeh Davaran, Sang Woo Joo, Nosratollah Zarghami, Younes Hanifehpour, Mohammad Samiei, Mohammad Kouhi and Kazem Nejati-Koshki, *Liposome: classification, preparation, and applications*. Nanoscale Research Letters, 2013. **8**(102): p. 1-9.
98. Kroon, J., et al., *Liposomal nanomedicines in the treatment of prostate cancer*. Cancer Treat Rev, 2014. **40**(4): p. 578-84.
99. Al-Azayzih, A., et al., *Liposome-mediated delivery of the p21 activated kinase-1 (PAK-1) inhibitor IPA-3 limits prostate tumor growth in vivo*. Nanomedicine, 2016. **12**(5): p. 1231-1239.
100. H. Maeda, J.W., T. Sawa, Y. Matsumura, K. Hori, *Tumor vascular permeability and the EPR effect in macromolecular therapeutics: a review*. Journal of Controlled Release, 2000. **65**: p. 271-284.
101. Prabhakar, U., et al., *Challenges and key considerations of the enhanced permeability and retention effect for nanomedicine drug delivery in oncology*. Cancer Res, 2013. **73**(8): p. 2412-7.
102. Rajesh L. Thangapazham, A.P., Shrikant Tele, Robert Blumenthal, Radha K. Maheshwar, *Evaluation of a nanotechnology based carrier for delivery of curcumin in prostate cancer cells*. Int J Oncol, 2008.
103. Sauvage, F., et al., *Formulation and in vitro efficacy of liposomes containing the Hsp90 inhibitor 6BrCaQ in prostate cancer cells*. Int J Pharm, 2016. **499**(1-2): p. 101-109.
104. Banerjee, R., et al., *Anisamide-targeted stealth liposomes: a potent carrier for targeting doxorubicin to human prostate cancer cells*. Int J Cancer, 2004. **112**(4): p. 693-700.
105. Pugazhendhi, A., et al., *Inorganic nanoparticles: A potential cancer therapy for human welfare*. Int J Pharm, 2018. **539**(1-2): p. 104-111.
106. He, X. and N. Ma, *An overview of recent advances in quantum dots for biomedical applications*. Colloids Surf B Biointerfaces, 2014. **124**: p. 118-31.
107. Singh, B.R., et al., *ROS-mediated apoptotic cell death in prostate cancer LNCaP cells induced by biosurfactant stabilized CdS quantum dots*. Biomaterials, 2012. **33**(23): p. 5753-67.
108. Lin, Z., et al., *A novel aptamer functionalized CuInS2 quantum dots probe for daunorubicin sensing and near infrared imaging of prostate cancer cells*. Anal Chim Acta, 2014. **818**: p. 54-60.
109. Garcia-Cortes, M., et al., *Sensitive prostate specific antigen quantification using dihydrolipoic acid surface-functionalized phosphorescent quantum dots*. Anal Chim Acta, 2017. **987**: p. 118-126.
110. Zhao, Y., et al., *Near-Infrared Quantum Dot and (89)Zr Dual-Labeled Nanoparticles for in Vivo Cerenkov Imaging*. Bioconjug Chem, 2017. **28**(2): p. 600-608.

111. Malekzad, H., et al., *Highly sensitive immunosensing of prostate specific antigen using poly cysteine capped by graphene quantum dots and gold nanoparticle: A novel signal amplification strategy*. Int J Biol Macromol, 2017. **105**(Pt 1): p. 522-532.
112. IGOR L. MEDINTZ, H.T.U., ALLEN R. GOLDMAN, AND HEDI MATTOUSSI, *Quantum dot bioconjugates for imaging,labelling and sensing*. nature materials, 2005. **4**.
113. Hooisweng Ow, D.R.L., Mamta Srivastava, Barbara A. Baird,Watt W. Webb, and Ulrich Wiesner, *Bright and Stable Core–Shell Fluorescent Silica Nanoparticles*. Nano Lett, 2005. **5**(1): p. 113-117.
114. Burns, A.A., et al., *Fluorescent silica nanoparticles with efficient urinary excretion for nanomedicine*. Nano Lett, 2009. **9**(1): p. 442-8.
115. Cui, D., et al., *Gastrin-releasing peptide receptor-targeted gadolinium oxide-based multifunctional nanoparticles for dual magnetic resonance/fluorescent molecular imaging of prostate cancer*. Int J Nanomedicine, 2017. **12**: p. 6787-6797.
116. Markus G. Lentschlg, P.R., Ursula L Rausch-Lentschlg,Thomas Allkemper,Michael Oelerlch, and Gerhard Laub, *Breath-hold Gadolinium-enhanced MR Angiography of the Major Vessels at 1.0 T: Dose-Response Findings and Angiographic Correlation*. Vascular and Interventional Radiology, 1998. **208**(2): p. 353-357.
117. Hu, F., et al., *High-performance nanostructured MR contrast probes*. Nanoscale, 2010. **2**(10): p. 1884-91.
118. Kaiyuan Ni, Z.Z., Zongjun Zhang, Zijian Zhou, Li Yang,Lirong Wang,Hua Ai,and Jinhao Gao, *Geometrical confined ultrasmall gadolinium oxide nanoparticles boost the T1 contrast ability*. Nanoscale 2016.
119. Gao, X., et al., *Mn-doped ZnSe d-dots-based alpha-methylacyl-CoA racemase probe for human prostate cancer cell imaging*. Anal Bioanal Chem, 2012. **402**(5): p. 1871-7.
120. Mijndonckx, K., et al., *Antimicrobial silver: uses, toxicity and potential for resistance*. Biometals, 2013. **26**(4): p. 609-21.
121. Yamada, M., M. Foote, and T.W. Prow, *Therapeutic gold, silver, and platinum nanoparticles*. Wiley Interdiscip Rev Nanomed Nanobiotechnol, 2015. **7**(3): p. 428-45.
122. Vlăsceanu, G.M., et al., *Silver nanoparticles in cancer therapy*. Nanobiomaterials in Cancer Therapy, 2016: p. 29-56.
123. Mohammadzadeh, R., *Hypothesis: silver nanoparticles as an adjuvant for cancertherapy*. Adv Pharm Bull, 2012. **2**(1): p. 133.
124. Firdhouse, M.J. and P. Lalitha, *Biosynthesis of silver nanoparticles using the extract of Alternanthera sessilis-antiproliferative effect against prostate cancer cells*. Cancer Nanotechnol, 2013. **4**(6): p. 137-143.
125. He, Y., et al., *Synthesis, characterization and evaluation cytotoxic activity of silver nanoparticles synthesized by Chinese herbal Cornus officinalis via environment friendly approach*. Environ Toxicol Pharmacol, 2017. **56**: p. 56-60.
126. Wang, H., et al., *Label-free electrochemical immunosensor for prostate-specific antigen based on silver hybridized mesoporous silica nanoparticles*. Anal Biochem, 2013. **434**(1): p. 123-7.
127. Anil Kumar, S.H., Xu Zhang, Juan Liu,† Aaron Tan,Shengliang Li, Shubin Jin, Xiangdong Xue, YuanYuan Zhao, Tianjiao Ji, Lu Han,Hong Liu, XiaoNing Zhang, Jinchao Zhang, Guozhang Zou, TianyouWang, Suoqin Tang, X and Xing-Jie Liang,, *Neuropilin-1-Targeted Gold Nanoparticles Enhance Therapeutic Efficacy of Platinum(IV) Drug for Prostate Cancer Treatment*. ACS Nano, 2014. **3**(5): p. 4205-4220.
128. Li, M., et al., *A novel signal amplification system fabricated immunosensor based on Au nanoparticles and mesoporous trimetallic PdPtCu nanospheres for sensitive detection of prostate specific antigen*. Sensors and Actuators B: Chemical, 2018. **261**: p. 22-30.
129. Zhang, B., et al., *Redox and catalysis 'all-in-one' infinite coordination polymer for electrochemical immunosensor of tumor markers*. Biosens Bioelectron, 2015. **64**: p. 6-12.

130. Spain, E., et al., *Detection of prostate specific antigen based on electrocatalytic platinum nanoparticles conjugated to a recombinant scFv antibody*. Biosens Bioelectron, 2016. **77**: p. 759-66.
131. Taylor, R.M. and L.O. Sillerud, *Paclitaxel-loaded iron platinum stealth immunomicelles are potent MRI imaging agents that prevent prostate cancer growth in a PSMA-dependent manner*. Int J Nanomedicine, 2012. **7**: p. 4341-52.
132. Chowdhury, P., et al., *Magnetic nanoformulations for prostate cancer*. Drug Discov Today, 2017. **22**(8): p. 1233-1241.
133. Brian Wan-Chi Tse, G.J.C., Carolina Soekmadji, Lidija Jovanovic, Raja S Vasireddy, Ming-Tat Ling, Aparajita Khatri, Tianqing Liu, Benjamin Thierry, and Pamela J Russell, *PSMA-targeting iron oxide magnetic nanoparticles enhance MRI of preclinical prostate cancer*. Nanomedicine, 2015. **10**(3): p. 375-386.
134. Agemy, L., et al., *Nanoparticle-induced vascular blockade in human prostate cancer*. Blood, 2010. **116**(15): p. 2847-56.
135. Carabineiro, S.A.C., *Applications of Gold Nanoparticles in Nanomedicine: Recent Advances in Vaccines*. Molecules, 2017. **22**(5).
136. Tedesco, S., et al., *Oxidative stress and toxicity of gold nanoparticles in Mytilus edulis*. Aquat Toxicol, 2010. **100**(2): p. 178-86.
137. Mie, G., *Beiträge zur Optik trüber Medien, speziell kolloidaler Metallösungen* Annalen der Physik, 1908.
138. El-Sayed, S.E.a.M.A., *Why gold nanoparticles are more precious than pretty gold: Noble metal surface plasmon resonance and its enhancement of the radiative and nonradiative properties of nanocrystals of different shapes*. Chemical Society Reviews, 2006. **35**: p. 209-217.
139. Prashant K. Jain, K.S.L., Ivan H. El-Sayed, and Mostafa A. El-Sayed, *Calculated Absorption and Scattering Properties of Gold Nanoparticles of Different Size, Shape, and Composition: Applications in Biological Imaging and Biomedicine*. J. Phys. Chem. B, 2006. **110**(14): p. 7238-7248.
140. Tiwari, B.P.a.A., *A Brief Review on the Application of Gold Nanoparticles as Sensors in Multi Dimensional Aspects*. Journal of Environmental Science, Toxicology and Food Technology, 2015. **1**(4): p. 01-07.
141. Rodriguez, C., et al., *Gold nanoparticle triggered dual optoplasmonic-impedimetric sensing of prostate-specific antigen on interdigitated porous silicon platforms*. Sensors and Actuators B: Chemical, 2018. **267**: p. 559-564.
142. Barbosa, A.I., et al., *Towards One-Step Quantitation of Prostate-Specific Antigen (PSA) in Microfluidic Devices: Feasibility of Optical Detection with Nanoparticle Labels*. Bionanoscience, 2017. **7**(4): p. 718-726.
143. Pal, M. and R. Khan, *Graphene oxide layer decorated gold nanoparticles based immunosensor for the detection of prostate cancer risk factor*. Anal Biochem, 2017. **536**: p. 51-58.
144. Suresh, L., et al., *Development of an electrochemical immunosensor based on gold nanoparticles incorporated chitosan biopolymer nanocomposite film for the detection of prostate cancer using PSA as biomarker*. Enzyme Microb Technol, 2018. **112**: p. 43-51.
145. Sattarahmady, N., A. Rahi, and H. Heli, *A signal-on built in-marker electrochemical aptasensor for human prostate-specific antigen based on a hairbrush-like gold nanostructure*. Sci Rep, 2017. **7**(1): p. 11238.
146. Srivastava, M., et al., *A comparative Study of Aptasensor Vs Immunosensor for Label-Free PSA Cancer Detection on GQDs-AuNRs Modified Screen-Printed Electrodes*. Sci Rep, 2018. **8**(1): p. 1923.
147. Vural, T., et al., *Electrochemical immunoassay for detection of prostate specific antigen based on peptide nanotube-gold nanoparticle-polyaniline immobilized pencil graphite electrode*. J Colloid Interface Sci, 2018. **510**: p. 318-326.
148. Kasten, B.B., et al., *Targeting prostate cancer cells with PSMA inhibitor-guided gold nanoparticles*. Bioorg Med Chem Lett, 2013. **23**(2): p. 565-8.
149. Ravi Shuklaa, N.C., Ajit Zambrea, Anandhi Upendran, Kavita Kattia, Rajesh R. Kulkarnia, Satish Kumar Nunea, Stan W. Castele, Charles Jeffrey Smitha, Jatin Vimalh, Evan Bootea, J. David Robertsond, Para

- Kani, Hendrik Engelbrechtg, Lisa D. Watkinsona, Terry L. Carmacka, John R. Levera, Cathy S. Cutlerd Charles Caldwellk, Raghuraman Kannana, and Kattesh V. Kattia, *Laminin receptor specific therapeutic gold nanoparticles (198AuNP-EGCg) show efficacy in treating prostate cancer*. PNAS, 2012. **109**(31): p. 12426–12431.
150. Li-Chu Tsai, H.-Y.H., Kun-Ying Lu, Sin-Yu Wang & Fwu-Long Mo, *EGCG/gelatin-doxorubicin gold nanoparticles enhance therapeutic efficacy of doxorubicin for prostate cancer treatment*. Nanomedicine, 2016. **11**(1): p. 9-30.
 151. Kim, W., et al., *Selective uptake of epidermal growth factor-conjugated gold nanoparticle (EGF-GNP) facilitates non-thermal plasma (NTP)-mediated cell death*. Sci Rep, 2017. **7**(1): p. 10971.
 152. Christian P. Nolsoe, S.T.-P., Flemming Burcharth, Thomas Horn, Soren Pedersen, Niels-Erik H. Christensen, Emil S. Obldag, Pia Haubro Andersen, Steen Karstrup, Torben Lorentzen, and Hans H. Holm,, *Interstitial hyperthermia of colorectal liver metastases with a US-guided Nd-YAG laser with a diffuser tip a pilot clinical study*. Radiology, 1993. **187**: p. 333-337.
 153. Oh, M.H., et al., *Genetically Programmed Clusters of Gold Nanoparticles for Cancer Cell-Targeted Photothermal Therapy*. ACS Appl Mater Interfaces, 2015. **7**(40): p. 22578-86.
 154. Jain, P.K., et al., *Review of Some Interesting Surface Plasmon Resonance-enhanced Properties of Noble Metal Nanoparticles and Their Applications to Biosystems*. Plasmonics, 2007. **2**(3): p. 107-118.
 155. Harmsen, S., et al., *Cancer imaging using surface-enhanced resonance Raman scattering nanoparticles*. Nat Protoc, 2017. **12**(7): p. 1400-1414.
 156. Mahan, M.M. and A.L. Doiron, *Gold Nanoparticles as X-Ray, CT, and Multimodal Imaging Contrast Agents: Formulation, Targeting, and Methodology*. Journal of Nanomaterials, 2018. **2018**: p. 1-15.
 157. A. W. Bosman, H.M.J., and E. W. Meijer, *About Dendrimers: Structure, Physical Properties, and Applications*. Chem. Rev., 1999. **99**: p. 1665-1688.
 158. A.TOMALIA, J.M.J.F.a.D., *Dendrimers and Other Dendritic Polymers*. Wiley & Sons Ltd, 2001.
 159. Yates, C.R. and W. Hayes, *Synthesis and applications of hyperbranched polymers*. European Polymer Journal, 2004. **40**(7): p. 1257-1281.
 160. Seiler, M., *Hyperbranched polymers: Phase behavior and new applications in the field of chemical engineering*. Fluid Phase Equilibria, 2006. **241**(1-2): p. 155-174.
 161. Donald A. Tomalia, D.M.H., and Michael S. Ferritto, *Comb-Burst Dendrimer Topology. New Macromolecular Architecture Derived from Dendritic Grafting*. Macromolecules, 1991. **24**: p. 1436-1438.
 162. Moller, M.G.a.M., *Uniform Highly Branched Polymers by Anionic Grafting: Arborescent Graft Polymers*. Macromolecules, 1991. **24**: p. 4548-4553.
 163. Tomalia, D.A., *The dendritic state*. Materials Today, 2005. **8**(3): p. 34-46.
 164. D'Emanuele, A. and D. Attwood, *Dendrimer-drug interactions*. Adv Drug Deliv Rev, 2005. **57**(15): p. 2147-62.
 165. Hildgen, R.S.D.a.P., *Synthesis and Evaluation of Novel Dendrimers with a Hydrophilic Interior as Nanocarriers for Drug Delivery*. Bioconjugate Chem, 2006. **17**: p. 29-41.
 166. Dufes, C., I.F. Uchegbu, and A.G. Schatzlein, *Dendrimers in gene delivery*. Adv Drug Deliv Rev, 2005. **57**(15): p. 2177-202.
 167. Lee, C.C., et al., *Designing dendrimers for biological applications*. Nat Biotechnol, 2005. **23**(12): p. 1517-26.
 168. Tom D. McCarthy, P.K., Scott A. Henderson, Michael Giannis, David F. O'Keefe, Graham Heery, Jeremy R. A. Paull, Barry R. Matthews, and George Holan, *Dendrimers as Drugs: Discovery and Preclinical and Clinical Development of Dendrimer-Based Microbicides for HIV and STI Prevention*. Molecular Pharmaceutics, 2005. **2**(4): p. 312-318.
 169. Robert G. Denkwalter, J.K., William J. Lukasavage, *Macromolecular Higjly Branched Homogeneous Comopund Based on Lysine Units*, U.S. Patent, Editor. 1981: USA.

170. D. A. TOMALIA, H.B., J. DEWALD, M. HALL, G. KALLOS, S. MARTIN, J. ROECK, J. RYDER, and P. SMITH, *A New Class of Polymers: Starburst-Dendritic Macromolecules*. *Polymer Journal*, 1985. **17**(1): p. 117-132.
171. Tam, J.P., *Synthetic peptide vaccine design: Synthesis and properties of a high-density multiple antigenic peptide system*. *Proc. Natl. Acad. Sci.*, 1988. **85**: p. 5401-5413.
172. Samal, S.K., et al., *Cationic polymers and their therapeutic potential*. *Chem Soc Rev*, 2012. **41**(21): p. 7147-94.
173. Scholl, M., et al., *The thermal polymerization of amino acids revisited; Synthesis and structural characterization of hyperbranched polymers from L-lysine*. *Journal of Polymer Science Part A: Polymer Chemistry*, 2007. **45**(23): p. 5494-5508.
174. Kadlecova, Z., et al., *DNA delivery with hyperbranched polylysine: a comparative study with linear and dendritic polylysine*. *J Control Release*, 2013. **169**(3): p. 276-88.
175. Mou, Q., et al., *Designing hyperbranched polymers for gene delivery*. *Molecular Systems Design & Engineering*, 2016. **1**(1): p. 25-39.
176. Svenson, S., *The dendrimer paradox--high medical expectations but poor clinical translation*. *Chem Soc Rev*, 2015. **44**(12): p. 4131-44.
177. Vial, J.-P.F.a.L., *Everything You Always Wanted to Know about Poly-L-lysine Dendrigrfts (But Were Afraid to Ask)*. HAL, 2018.
178. Ioannis Tsogas, T.T., Zili Sideratou, Constantinos M. Paleos, Helene Collet, Jean Christophe Rossi, Bernard Romestand, and Auguste Commeyras, *Interaction and Transport of Poly(L-lysine) Dendrigrfts through Liposomal and Cellular Membranes: The Role of Generation and Surface Functionalization*. *Biomacromolecules*, 2007. **8**: p. 3263-3270.
179. Wittrup, A. and J. Lieberman, *Knocking down disease: a progress report on siRNA therapeutics*. *Nat Rev Genet*, 2015. **16**(9): p. 543-52.
180. Cornelius, J., et al., *Endoplasmic reticulum oxidoreductase 1 alpha modulates prostate cancer hallmarks*. *Transl Androl Urol*, 2021. **10**(3): p. 1110-1120.
181. Liu, W., et al., *PRPF6 promotes androgen receptor/androgen receptor-variant 7 actions in castration-resistant prostate cancer cells*. *Int J Biol Sci*, 2021. **17**(1): p. 188-203.
182. Dirk Strumberg, B.S., Ulrich Traugott, Christiane Vank, Ansgar Santel, Oliver Keil, Klaus Giese, Jörg Kaufmann and Joachim Dreves, *Phase I clinical development of Atu027, a siRNA formulation targeting PKN3 in patients with advanced solid tumors*. *International Journal of Clinical Pharmacology and Therapeutics*, 2012. **50**(1): p. 76-78.
183. Tabernero, J., et al., *First-in-humans trial of an RNA interference therapeutic targeting VEGF and KSP in cancer patients with liver involvement*. *Cancer Discov*, 2013. **3**(4): p. 406-17.
184. Guo, J., et al., *Biomimetic nanoparticles for siRNA delivery in the treatment of leukaemia*. *Biotechnol Adv*, 2014. **32**(8): p. 1396-409.
185. Mu, X., et al., *Doxorubicin and PD-L1 siRNA co-delivery with stem cell membrane-coated polydopamine nanoparticles for the targeted chemoimmunotherapy of PCa bone metastases*. *Nanoscale*, 2021.
186. Oner, E., et al., *Development of EphA2 siRNA-loaded lipid nanoparticles and combination with a small-molecule histone demethylase inhibitor in prostate cancer cells and tumor spheroids*. *J Nanobiotechnology*, 2021. **19**(1): p. 71.
187. Jeffrey S. Ross, C.E.S., Hugh A. G. Fisher, Ronald P. Kaufman, Jr., Prabhjot Kaur, Karen Gray, Iain Webb Gary S. Gray, Rebecca Mosher, and Bhaskar V. S. Kallakury, *Correlation of Primary Tumor Prostate-Specific Membrane Antigen Expression with Disease Recurrence in Prostate Cancer*. *Clinical Cancer Research*, 2003. **9**: p. 6357-6362.
188. Ghosh, A. and W.D. Heston, *Tumor target prostate specific membrane antigen (PSMA) and its regulation in prostate cancer*. *J Cell Biochem*, 2004. **91**(3): p. 528-39.

189. Gerald P. Murphy, A.-A.A.E., Sai L. Su, David G. Bostwick, and Eric H. Holmes, *Current Evaluation of the Tissue Localization and Diagnostic Utility of Prostate Specific Membrane Antigen*. American Cancer Society, 1998. **83**(11): p. 2259-2269.
190. Yao, V., et al., *Expression of prostate-specific membrane antigen (PSMA), increases cell folate uptake and proliferation and suggests a novel role for PSMA in the uptake of the non-polyglutamated folate, folic acid*. Prostate, 2010. **70**(3): p. 305-16.
191. Yao, V. and D.J. Bacich, *Prostate specific membrane antigen (PSMA) expression gives prostate cancer cells a growth advantage in a physiologically relevant folate environment in vitro*. Prostate, 2006. **66**(8): p. 867-75.
192. Low, C.P.L.A.P.S., *Delivery of macromolecules into living cells: A method that exploits folate receptor endocytosis*. Proc. Nadl. Acad. Sci., 1991. **88**: p. 5572-5576.
193. Christopher P. Leamon, J.A.R., Iontcho R. Vlahov, Marilyn Vetzal, Nikki Parker, and L.-C.X. Jeffrey S. Nicoson, and Elaine Westrick, *Synthesis and Biological Evaluation of EC72: A New Folate-Targeted Chemotherapeutic*. Bioconjugate Chem, 2005. **16**(4): p. 803-811.
194. Henne, W.A., et al., *Synthesis and activity of a folate peptide camptothecin prodrug*. Bioorg Med Chem Lett, 2006. **16**(20): p. 5350-5.
195. Flores, O., et al., *PSMA-Targeted Theranostic Nanocarrier for Prostate Cancer*. Theranostics, 2017. **7**(9): p. 2477-2494.
196. Maruyama, T., Y. Fujimoto, and T. Maekawa, *Synthesis of gold nanoparticles using various amino acids*. J Colloid Interface Sci, 2015. **447**: p. 254-7.
197. Alkilany, A.M. and C.J. Murphy, *Toxicity and cellular uptake of gold nanoparticles: what we have learned so far?* J Nanopart Res, 2010. **12**(7): p. 2313-2333.
198. Yah, C.S., *The toxicity of Gold Nanoparticles in relation to their physiochemical properties*. Biomedical Research, 2013. **24**(3): p. 400-413.
199. Suk, J.S., et al., *PEGylation as a strategy for improving nanoparticle-based drug and gene delivery*. Adv Drug Deliv Rev, 2016. **99**(Pt A): p. 28-51.
200. Shin, H., et al., *Quantifying the level of nanoparticle uptake in mammalian cells using flow cytometry*. Nanoscale, 2020. **12**(29): p. 15743-15751.
201. Hattori, Y. and Y. Maitani, *Folate-linked lipid-based nanoparticle for targeted gene delivery*. Curr Drug Deliv, 2005. **2**(3): p. 243-52.
202. Guo, S. and L. Huang, *Nanoparticles Escaping RES and Endosome: Challenges for siRNA Delivery for Cancer Therapy*. Journal of Nanomaterials, 2011. **2011**: p. 1-12.
203. Zhang, X.Q., et al., *Interactions of nanomaterials and biological systems: Implications to personalized nanomedicine*. Adv Drug Deliv Rev, 2012. **64**(13): p. 1363-84.
204. Fitzgerald, K.A., et al., *Anisamide-targeted gold nanoparticles for siRNA delivery in prostate cancer - synthesis, physicochemical characterisation and in vitro evaluation*. J Mater Chem B, 2016. **4**(13): p. 2242-2252.